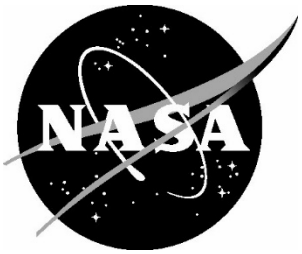
NASA/TP–20260008724



Lunar Dust Vacuum Cleaner Status Report

Steve A. Lee
NASA Johnson Space Center, Houston, Texas

Glenn Waguespack
Amentum, Chantilly, Virginia

Kristen John
NASA Johnson Space Center, Houston, Texas

October 2026

NASA STI Program Report Series

Since its founding, NASA has been dedicated to the advancement of aeronautics and space science. The NASA scientific and technical information (STI) program plays a key part in helping NASA maintain this important role.

The NASA STI program operates under the auspices of the Agency Chief Information Officer. It collects, organizes, provides for archiving, and disseminates NASA's STI. The NASA STI program provides access to the NTRS Registered and its public interface, the NASA Technical Reports Server, thus providing one of the largest collections of aeronautical and space science STI in the world. Results are published in both non-NASA channels and by NASA in the NASA STI Report Series, which includes the following report types:

- TECHNICAL PUBLICATION. Reports of completed research or a major significant phase of research that present the results of NASA Programs and include extensive data or theoretical analysis. Includes compilations of significant scientific and technical data and information deemed to be of continuing reference value. NASA counterpart of peer-reviewed formal professional papers but has less stringent limitations on manuscript length and extent of graphic presentations.

- TECHNICAL MEMORANDUM. Scientific and technical findings that are preliminary or of specialized interest, e.g., quick release reports, working papers, and bibliographies that contain minimal annotation. Does not contain extensive analysis.

- CONTRACTOR REPORT. Scientific and technical findings by NASA-sponsored contractors and grantees.

- CONFERENCE PUBLICATION. Collected papers from scientific and technical conferences, symposia, seminars, or other meetings sponsored or co-sponsored by NASA.

- SPECIAL PUBLICATION. Scientific, technical, or historical information from NASA programs, projects, and missions, often concerned with subjects having substantial public interest.

- TECHNICAL TRANSLATION. English-language translations of foreign scientific and technical material pertinent to NASA's mission.

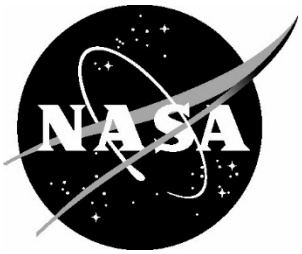
Specialized services also include organizing and publishing research results, distributing specialized research announcements and feeds, providing information desk and personal search support, and enabling data exchange services.

For more information about the NASA STI program, see the following:

- Access the NASA STI program home page at http://www.sti.nasa.gov

.

NASA/TP–20260008724



Lunar Dust Vacuum Cleaner Status Report

Steve A. Lee
NASA Johnson Space Center, Houston, Texas

Glenn Waguespack
Amentum, Chantilly, Virginia

Kristen John
NASA Johnson Space Center, Houston, Texas

National Aeronautics and
Space Administration

Johnson Space Center
Houston, Texas

October 2026

The use of trademarks or names of manufacturers in this report is for accurate reporting and does not constitute an official endorsement, either expressed or implied, of such products or manufacturers by the National Aeronautics and Space Administration.

Available from:

NASA STI Program / Mail Stop 050
NASA Langley Research Center
Hampton, VA 23681-2199

TABLE OF CONTENTS

Abstract……11

1 Background and Related Work 11

1.1 Vacuum Cleaners Specific to Space Flight 11

1.1.1 Lunar Dust Vacuum Cleaners 11

1.1.2 Non-Lunar Dust Vacuum Cleaners 12

2 Analysis Techniques 14

2.1 Scanning Electron Microscope (SEM) with Imaging Analysis (JSC/B13) 14

2.2 Particle Analyzer Utilizing Light Diffraction (Microtrac, B31 MEGA Lab) 15

2.3 Mass Measurements 17

3 Fabrication of New Test Samples 17

3.1 Description 17

3.2 Mitigation of Uncertainty 17

3.2.1 Controlling Stretch of Fabric 17

3.2.2 Managing Loose Threads 18

3.3 Procedure for Fabricating New Samples 19

4 Loading of Test Samples with Simulant 21

4.1 Description 21

4.1.1 Selection of Simulant 21

4.1.2 Selection of Deposition Method 21

4.2 Mitigation of Uncertainty 22

4.2.1 Inconsistent Loading (Distribution) 22

4.2.2 Inconsistent Loading (Mass/Layers) 23

4.2.3 Initial Adhesion and Cohesion 25

4.3 Procedure for Loading Samples 25

5 Particulate Removal by Airflow (Vacuum Cleaner Testing) 27

5.1 Description 27

5.2 Mitigation of Uncertainty 27

5.2.1 Inconsistent Vacuuming (Position) 27

5.2.2 Inconsistent Vacuuming (Speed) 28

5.2.3 Inconsistent Vacuuming (Flow Rate) 28

5.2.4 Recording of Time 28

5.3 Procedure for Testing 28
5.4 Test Results 29
6 Predictive Model 30
6.1 List of Symbols 31
6.2 Rock'n'Roll Resuspension Model ([RH], [Biasi], [Vincent]) 32
6.3 Numerical Algorithm 38
6.4 Friction Velocity 41
6.5 Model Notes 42
6.6 Comparison of Model Results with Published Rock'n'Roll Model Output 42
6.7 Variation of Pressure on Modeled Particle Resuspension 49
7 References 50
8 Recommendation for Future Work 51
9 Acknowledgements 52
10 Appendix 53
10.1 Assessment Memo from Building 13 Microscopy Lab 53

LIST OF FIGURES AND TABLES

Figure 1. Vacuum Brush Assembly (Apollo 11 and 12) 11
Figure 2. Hand-Held Vacuum Cleaner from Apollo Missions 12
Figure 3. Vacuum Cleaner Test Set-up From 2009 12
Figure 4. ISS Wet/Dry Vacuum Specifications 133
Figure 5. ISS COTS Vacuum Specifications 13
Figure 6. Makita Vacuum Cleaner 13
Figure 7. Color-Coded Element Map from Building 13 Microscopy Lab 15
Figure 8. Particle Count Distribution from Building 13 Microscopy Lab 15
Figure 9. Microtrac Bluewave S3500 Particle Size Analyzer 16
Figure 10. Particle Size Distribution of Lunar Simulants (measured in B31 Lab) 16
Figure 11. Mass Balance 17
Figure 12. Cutting Pattern for Gold-Kapton Tape 20
Figure 13. Ortho-Fabric Sample with Gold-Kapton Masking 20
Figure 14. Simulant Loading Device (SLD) 22
Figure 15. Comparison of Loading Distribution from Different Methods 23
Figure 16. Simulant Deposited on Fabric Samples 24
Figure 17. Dust Penetrated Through Ortho fabric 24
Figure 18. Sample Preparation Setup 25
Figure 19. Finished Product (200 grinding cycles) 26
Figure 20. Vacuum Testing Setup 29
Figure 21. Percent Simulant Removed as Function of Time 30
Figure 22. Moment balance for rolling resuspension model (reproduced from Vincent et. al. 2019) 33
Figure 23. Comparison of Python model output with Reeks and Hall model results for fraction of remaining 10 μm diameter alumina particles on a polished stainless steel surface after 1 second of exposure to a constant friction velocity flow. “New (RH Table 4)” uses input adhesion parameters from Table 4 of Biasi et. al., 2001. “New (Biasi corr.)” uses input adhesion parameters via application of a correlation from Biasi, et al. (2001). 43
Figure 24. Comparison of Python model output with Reeks and Hall [RH] model results for fraction of remaining 20 μm diameter alumina particles on a polished stainless steel surface after 1 second of exposure to a constant friction velocity flow. “New (RH Table 4)” uses input adhesion parameters from Table 4 of [RH]. “New (Biasi corr.)” uses input adhesion parameters via application of a correlation from Biasi, et al. (2001) [Biasi]. 44

Figure 25. Comparison of Python model output with Reeks and Hall [RH] model results for fraction of remaining 13 μm diameter graphite particles on a polished stainless steel surface after 1 second of exposure to a constant friction velocity flow. “New (RH Table 4)” uses input adhesion parameters from Table 4 of [RH]. “New (Biasi corr.)” uses input adhesion parameters via application of a correlation from Biasi, et al. (2019) [Biasi]. 44

Figure 26. Comparison of Python model output with Biasi, et al. (2001) model results for fraction of graphite particles resuspended from a polished stainless steel surface by 1 second of exposure to a constant friction velocity flow, assuming a surface adhesion energy of 0.15 J/m^2.45

Figure 27. Comparison of Python model output with Biasi, et al. (2001) model results for fraction of graphite particles resuspended from a polished stainless steel surface by 1 second of exposure to a constant friction velocity flow, assuming a surface adhesion energy of 0.56 J/m^2.46

Figure 28. Comparison of Python model output with Biasi, et al. (2001) model results for fraction of 20 μm diameter alumina particles resuspended from a polished stainless steel surface by 1 second of exposure to a constant friction velocity flow, assuming a surface adhesion energy of 0.56 J/m^2. 46

Figure 29. Comparison of Python model output with Biasi, et al. (2001) model results for fraction of 30 μm diameter glass microballoons resuspended from a glass surface by 1 second of exposure to a constant friction velocity flow, assuming a surface adhesion energy of 0.56 J/m^2.47

Figure 30. Comparison of Python model output with Biasi, et al. (2001) model results for fraction of 6.37 μm diameter metalic zinc particles resuspended from a flat surface by 1 second of exposure to a constant friction velocity flow, assuming a surface adhesion energy of 0.56 J/m^2. 47

Figure 31. Comparison of Python model output with Vincent, et al. (2019) results for fraction of 9.2 μm diameter glass particles resuspended from a doped silicon surface by exposure to a time-varying friction velocity flow. Since Vincent does not specify input surface adhesion energy, two values are used in the Python model. 48

Figure 32. Variation of particle resuspension fraction with gas pressure, subject to the assumed inputs from Table 4. 50

Table 1. Sets of Test Samples Created with the Simulant Loading Device 26

Table 2. Test Point Durations 29

Table 3. Inputs for Particle Resuspension Pressure Dependency Analysis 50

LIST OF ACRONYMS AND ABBREVIATIONS

ARS	Air Revitalization System
BVAD	Baseline Values and Assumptions Document
CHC	Carbon Dioxide and Humidity Control
CTSD	Crew and Thermal Systems Division
ECLSS	Environmental Control and Life Support System
EVA	Extravehicular Activity
HLS	Human Landing System
HSIR	Human Systems Integration Requirements
IMV	Inter-Modular Ventilation
IRD	Interface Requirements Document
ISS	International Space Station
JSC	Johnson Space Center
MPCV	Multi Purpose Crew Vehicle
PCS	Pressure Control System
PPCO2	Partial Pressure of Carbon Dioxide
PPO2	Partial Pressure of Oxygen
PSRD	Program System Requirements Document
RH	Relative Humidity
SRD	System Requirements Document

Abstract

This report documents the development, execution, and analysis of a lunar dust vacuum cleaner test campaign performed to better understand particulate removal from space suit materials in support of future Artemis missions. The work includes fabrication of representative Ortho fabric test coupons, controlled loading of lunar simulants using a repeatable simulant loading device, and vacuum-based particulate removal testing under defined flow and contamination conditions. Multiple sources of uncertainty associated with sample preparation, simulant distribution, penetration depth, adhesion, cohesion, and vacuuming parameters were identified and mitigated through refined procedures and measurement techniques. Post-test analysis relied primarily on high-precision mass measurements, supplemented by microscopy assessments to characterize particle distribution and limitations of available analytical tools. A predictive particle resuspension model based on the Reeks and Hall "Rock'n'Roll" framework was implemented to complement experimental results, including verification against published data and evaluation of parameter sensitivity. Together, the experimental and modeling outcomes provide insight into removal efficiency trends, repeatability improvements, and the influence of contamination and flow variables. These results inform recommendations for future testing, operational considerations, and vacuum system design for effective lunar dust management.

1 Background and Related Work

1.1 Vacuum Cleaners Specific to Space Flight

1.1.1 Lunar Dust Vacuum Cleaners

1.1.1.1 Vacuum Cleaner on Apollo missions

There were two vacuum cleaners that were used during the Apollo missions. The first vacuum cleaner, named "vacuum brush assembly" in the Apollo Experience Report (see Figure 1), was part of the environmental control system and was used on Apollo 11 and 12. This vacuum cleaner reportedly did not work well and it was replaced with a portable vacuum cleaner based on the suit loop compressor (see Figure 2). While this second version of the vacuum cleaner worked better than the first, it had documented clogging problems and still didn't remove all of the dust from the surfaces to be cleaned.

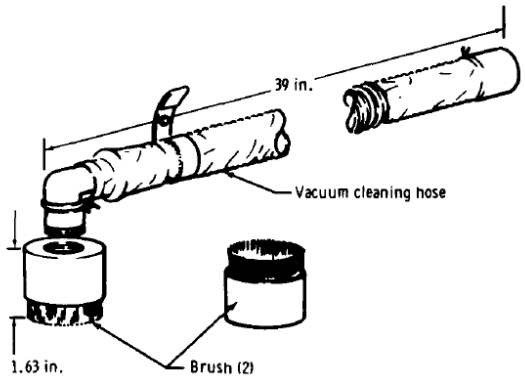


Figure 1. Vacuum Brush Assembly (Apollo 11 and 12)

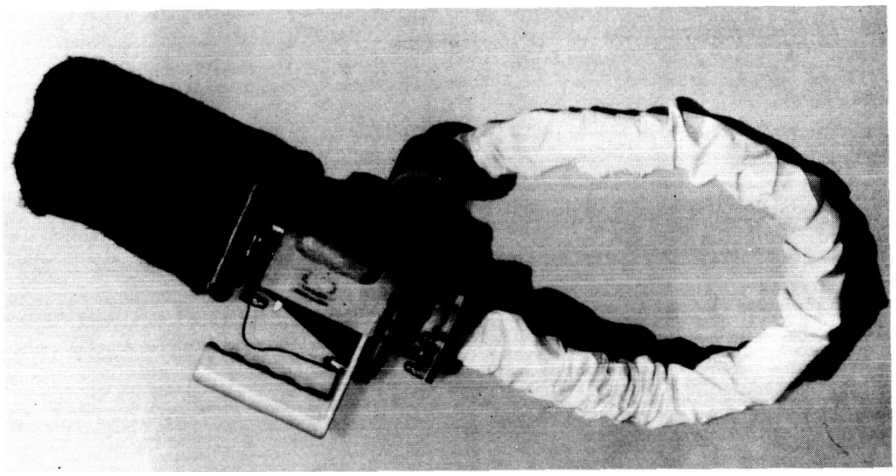


Figure 2. Hand-Held Vacuum Cleaner from Apollo Missions

1.1.1.2 2010 Vacuum Cleaner Testing

Between 2009 and 2010, three tests were conducted, two at normal atmosphere and one in a vacuum chamber in building 7 at 10.2 psia and 8.3 psia, using JSC-1AF simulant. The test setup is shown in Figure 3. Surface materials, flow rate, vacuum tool attachment, and atmosphere pressure were varied for these tests. Mass of the test samples were recorded before and after cleaning. Particulate removal is a function of flow rate and pressure were inconclusive due to the inability to identify patterns in the results.



Figure 3. Vacuum Cleaner Test Set-up From 2009

1.1.2 Non-Lunar Dust Vacuum Cleaners

1.1.2.1 ISS Vacuum Cleaners

Three vacuum cleaners are currently certified for ISS use. The first is a custom, brushless motor vacuum cleaner designed for both wet and dry operation (used on Shuttle and ISS). Photo and specifications are shown in Figure 4. The second is a COTS brushed motor vacuum cleaner made by Oreck (Model BB1200DB-R). A picture and specifications are shown in Figure 5. The third, and most recently certified, a cordless/portable brushless motor COTS vacuum cleaner made by Makita (Model XCV09Z). Photo is shown in Figure 6.



Characteristic	High	Low
Suction restricted inlet	27.0 inH_2O	9.1 inH_2O
Inlet air velocity	N/A	N/A
Blower speed *	11400 RPM	10700 RPM
Blower speed max @ 120 VDC *	12500 RPM	N/A
Heat rejections	N/A	N/A
External Touch Temperature after 30 Min.	80 °F	N/A
Bag delta pressure	N/A	N/A
Motor operating life	10,000 hours (continuous use) or 22 years adjusted for normal use	N/A
Power draw from utility outlets (@ 120 VDC)	2.27 A	0.75 A
Bag rating (size of particle)	6 microns	N/A
Bag capacity (liquid)	24 oz	N/A
Bag volume (dry capacity)	100 in^3	N/A
Bag shelf-life	None	N/A

Figure 4. ISS Wet/Dry Vacuum Specifications



Performance Characteristics

Characteristic	High	Low
Lift (inches of water) - Dead Head	69.3 inH_2O	
Lift (inches of water) - Free Flow	10.9 inH_2O	
Inlet air velocity	773 ft./min	
Air flow	67.5 cfm	
Power draw from utility outlets (@ 120 VDC)	660 W	
Bag capacity (liquid)	N/A	N/A
Bag volume (dry capacity)	168 in^3	N/A
Bag shelf-life	N/A	N/A

Figure 5. ISS COTS Vacuum Specifications



Figure 6. Makita Vacuum Cleaner

2 Analysis Techniques

2.1 Scanning Electron Microscope (SEM) with Imaging Analysis (JSC/B13)

The microscopy lab in Building 13 at JSC has an Electron Microscope with X-Ray Dispersive Spectroscopy, coupled with image analysis software. This system provides the ability to perform surface particle counting. Ortho fabric samples loaded with LHS-1D simulant were sent to the microscopy lab for a preliminary analysis and assessment of capabilities to determine the results would meet the needs of the project. A memo received from James Martinez, a lead technologist in the lab, gave details on this analysis and assessment. A copy of the memo is provided in the Appendix Section 10.1.

The ability to identify elemental composition and particle count was demonstrated. A set of color-coded microscopy images from the analysis is shown in Figure 7. Each color represents a different element identified with the spectroscopy analysis. Also, a histogram of the particle count distribution is shown in Figure 8. Unfortunately, the accuracy of the particle size distribution (PSD) and the total particle count were not verified. The main reason for not using the lab for analysis was the time and effort required to obtain particle count results, requiring approximately 30 minutes to analyze 1 mm^2 of sample surface area. A list of the most significant pros and cons is shown below.

- Pros
    - Elemental analysis
    - High resolution
- Cons
    - Slow data acquisition
    - Particles may move due to charge
    - Each element must be analyzed individually
    - Ortho fabric susceptible to damage

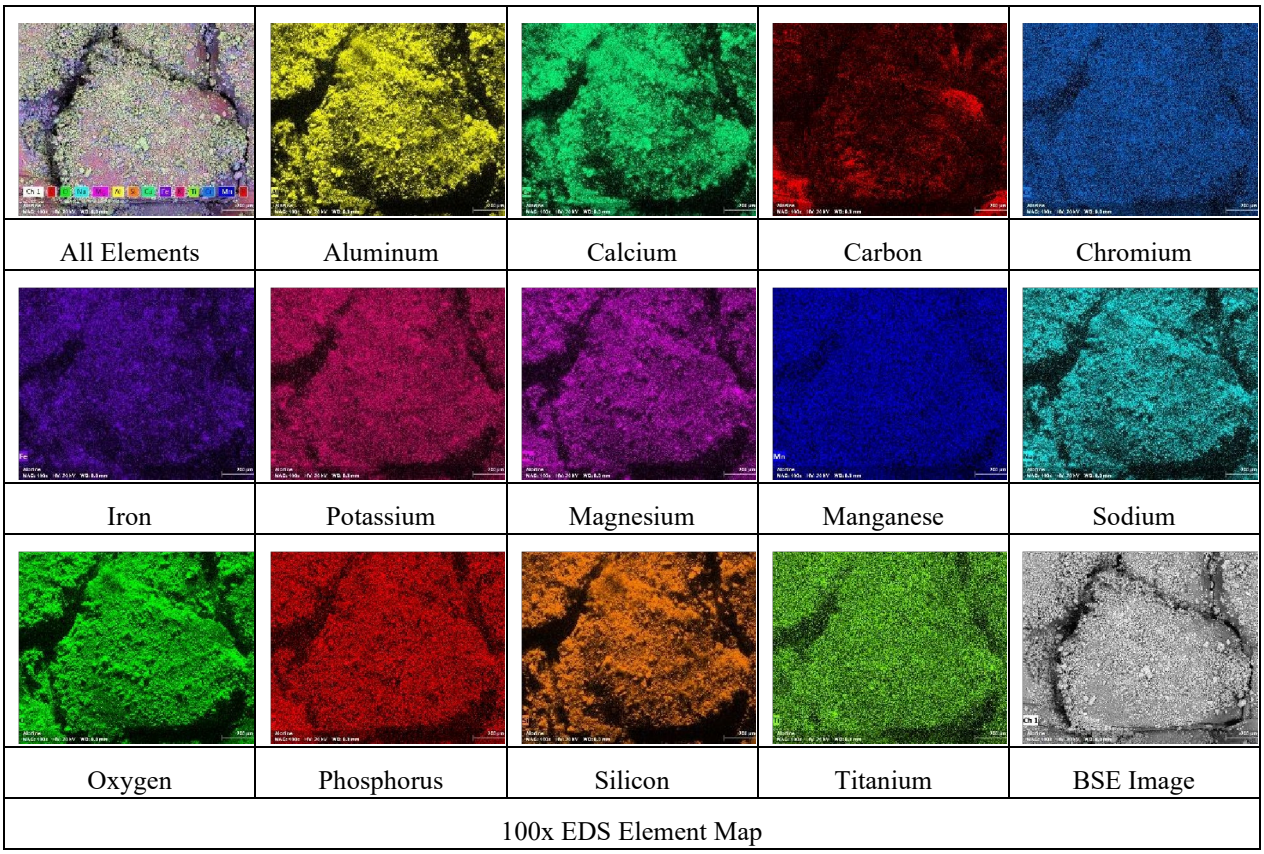
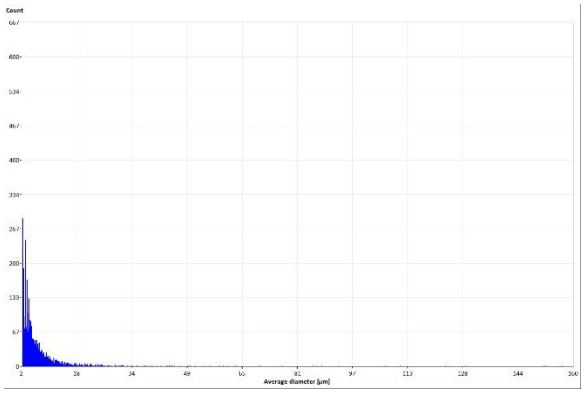


Figure 7. Color-Coded Element Map from Building 13 Microscopy Lab

Feature analysis	Field 0	
fields	1	
Image	1024 x 768	pixels
Area	921881	µm²
Particles	4369	
Accepted	4369	

Particle Count Results



Histogram of Particle Ave. Diameter (µm)

Figure 8. Particle Count Distribution from Building 13 Microscopy Lab

2.2 Particle Analyzer Utilizing Light Diffraction (Microtrac, B31 MEGA Lab)

The Bluewave S3500 particle analyzer (Figure 9) by Microtrac, Inc. was located in building 31, room 2020. This device could determine particle size distribution of particles suspended in a

liquid in the range of 0.1 microns to 3000 microns. The particle size distributions from lunar simulants measured with the blue wave particle analyzer is shown in Figure 10. This clearly shows that the BP-1 simulant was skewed towards particles with larger sizes. This was one of the main reasons for using LHS 1D for our testing. The blue wave particle analyzer would have been used to analyze the sample coupons after testing; however, the analyzer required a minimum of 0.5 grams in order to perform an analysis. Since the test samples would have approximately 20 to 40 milligrams of dust before testing, this ruled out the Bluewave particle analyzer as a post-test analysis option.



Figure 9. Microtrac Bluewave S3500 Particle Size Analyzer

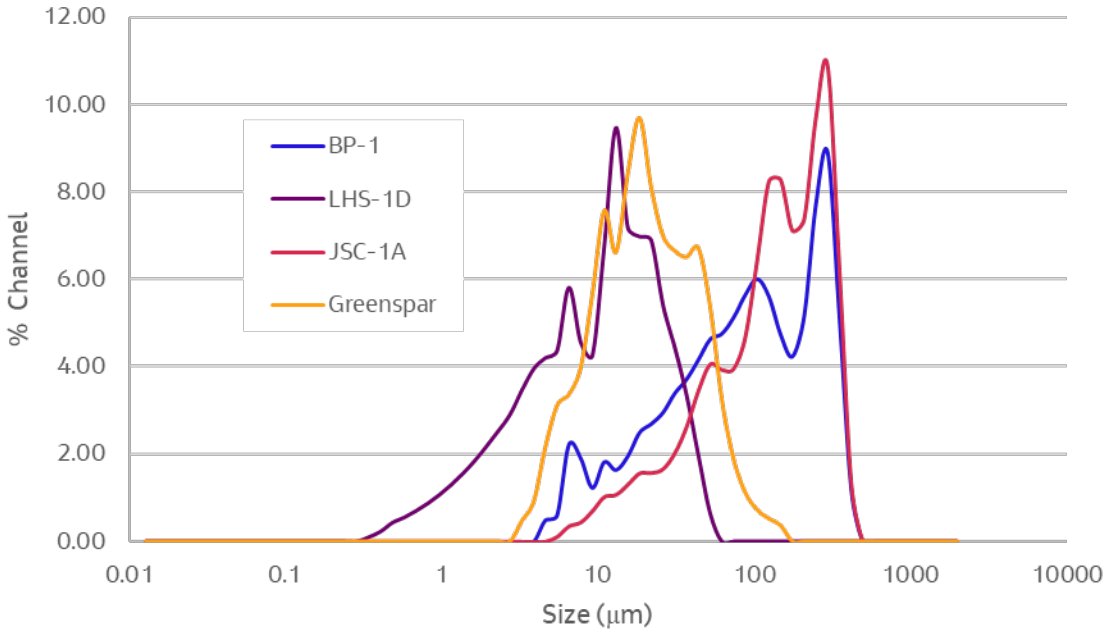


Figure 10. Particle Size Distribution of Lunar Simulants (measured in B31 Lab)

2.3 Mass Measurements

While the intention was to have a significant portion of analysis be from particle analyzers, the majority of post-test analysis was performed by a mass balance. Since it was known that the amount of mass remaining on the test coupon after testing could be as low as 1 mg, a mass balance (Mettler Toledo) with a readability of 0.002 mg was purchased. This greatly increased the capabilities of precise measurements in the lab. A picture of the mass balance is shown in Figure 11.

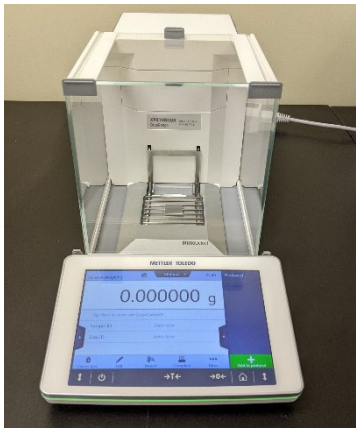


Figure 11. Mass Balance

3 Fabrication of New Test Samples

3.1 Description

The material samples used in the vacuum cleaner testing were to have the following properties:

- Material: Ortho fabric. We chose to focus on testing the Ortho fabric since this was expected to be the most challenging surface to both contaminate and clean. Other surfaces (buttons, switches, flat smooth surface of interior cabin) were not as much of a challenge as the woven fabric.
- Exposed area to be cleaned: 1.25” x 0.5”. This was sized to match the shape and area of the entrance of the nozzle tool used in testing. A larger area was considered; however, this was good for baseline testing because it didn't have the complexities associated with movement of the nozzle tool.

3.2 Mitigation of Uncertainty

To limit the amount of uncertainty in the test results, the development of the test coupons needed to be both controllable and repeatable. Some of the potential sources of uncertainty that were identified and mitigated against are shown below.

3.2.1 Controlling Stretch of Fabric

Stretching the fabric causes open fibers, which changes the configuration. Unstretched (loose or relaxed) fabric could have higher penetration of simulant due to gaps opening up between the

fibers. Stretched fabric could have less penetration of simulant because the gaps could become constricted. Cutting with scissors requires handling, which could cause some inadvertent stretching. Laser cutting solved this problem because the material was laid flat during the cutting process and the cutter did not pull on the fabric while cutting. The laser cutter also ensured very consistent and accurate cuts.

3.2.2 Managing Loose Threads

Initially, the test coupons were fabricated by cutting the Ortho fabric samples with scissors. This process left frayed ends and fabric threads that could be easily pulled from the fabric coupon. It was observed that if a fabric thread inadvertently was removed from the coupon, this could cause uncertainties in the final mass measurements, which needed to be accurate to less than 1 mg, based on preliminary tests. Laser-cutting helped to control the frayed edges. However, it was determined that the edges of the coupon still needed to be sealed in order to prevent any threads from being removed from the coupon. Therefore, several techniques were evaluated. These are described below.

Gental 101 (General Plastics North Corp., JSC SDS 24455) is a material that is much like superglue, and it is used by the Softgoods Lab when they cut Ortho fabric and want to prevent threads from fraying. This didn't work for us because the Gental 101 material is designed to wick into the fabric material. The distance that the fluid wicked into the material could not be precisely controlled. Therefore, we could not be certain that the Gental 101 would not wick into an area that we desire to be contaminated with lunar simulant.

Heat sealing was tried, but the threads would not fuse together. They require a much higher temperature than could be produced from our heat sealer. This is not entirely unexpected since the Ortho fabric is a material for the exterior layer of the xEMU suit, which must perform in very high temperatures (>250°F).

Hot glue was tried, but much like the Gental 101, the coverage area could not be precisely controlled. It also left a lip next to the exposed area that seems thicker than desired. Additionally, the hot glue would likely have adhered to lunar simulant.

It was ultimately decided that masking the uncontaminated areas with tape was the preferred method. However, many of the tapes considered were not used for different reasons. Some of the tapes used did not have enough adhesion to the Ortho fabric, and the adhesion to the front and back sides of the Ortho fabric were not always consistent. Since the front and back sides of the Ortho fabric are different materials, the adhesive on the tapes performed differently on each side. If the tape did not adhere to the Ortho fabric properly, simulant could collect underneath the tape, preventing it from being removed by the vacuum cleaner. Some of the tape adhesives were too strong, making them very difficult to work with. The tape performance needed to be observed for a few days because at least one of the tapes that initially showed good adhesion performance was loosened from the Ortho fabric after a couple of days.

The method of applying the tape to the fabric was important. If there wasn’t enough pressure evenly applied during application of the tape, the tape did not adhere properly in many cases.

Metal rollers were used to apply pressure to the tape while fabricating the coupons. A 1-inch-wide roller and ¼-inch wide roller were used for large and detailed areas, respectively.

The non-adhesive side of the tape was important as well. This side of the tape needed to have poor adhesion with the lunar simulant. A smooth, glossy surface, such as that with the gold-Kapton tape, was preferred. Other tapes had more textured surfaces, like that of paper, which retained some of the simulant it came into contact with. Since the simulants seemed to have poor adhesion with smooth metal surfaces, the fact that the gold-Kapton tape had a metal surface was beneficial. It should be noted that regular Kapton tape also had poor adhesion with the simulant. However, the regular Kapton tape was not available in the 2-inch width that was desired for manufacturing with the laser cutter because the pattern could be cut with a single strip of tape. A smaller-width tape would need to be applied to the Ortho fabric in two pieces, which would create a seam where unwanted simulant could collect and potentially cause unwanted uncertainties in the test results.

3.3 Procedure for Fabricating New Samples

A laser cutter was used to cut Ortho fabric into rectangles and to cut gold-Kapton tape, adhered to release paper, into the pattern shown in Figure 13 below. To manufacture the samples, Ortho fabric was laser-cut to 1.75” x 1.0” rectangles. Also, gold-Kapton tape[1] was placed in strips on release paper and then laser-cut in a pattern, shown in Figure 12. Transfer tape was then used to transfer the gold-Kapton tape to the Ortho fabric, using a template for positioning. Metal rollers were used to ensure that the tape was adequately adhered to the Ortho fabric. The tape was then folded over the edges to match the shape of the Ortho fabric rectangle. The protective polymer film was trimmed from the edges, leaving only the part covering the top face of the Ortho fabric.

[1] It should be noted that gold-Kapton tape is expensive and not widely used, but after testing many different types of tapes (both purchased and available in our labs), this tape was chosen because it was the best performing tape that was available. It is expected that research to find a replacement tape with the same properties mentioned would result in a more economical choice. However, the tape would need to be ordered from a manufacturer of technical tape (such as 3M) with specifications for adhesion on the sticky and non-sticky sides of the tape.

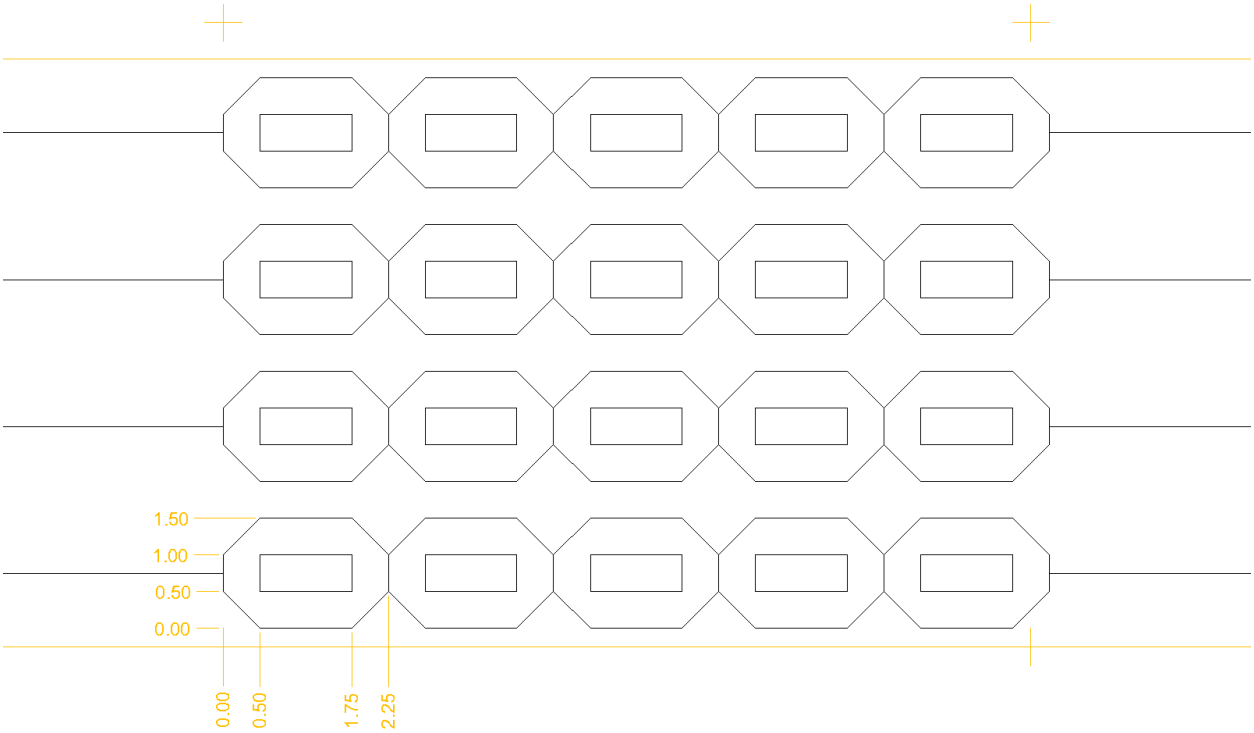


Figure 12. Cutting Pattern for Gold-Kapton Tape

Masking tape was then cut into a pattern, shown in the figure, and then positioned and attached on top of the sample. The purpose of the masking tape was to keep the samples secure during loading, and to be a means to easily remove the polymer film after loading.

Next, the polymer film and the masking tape were then removed to enable mass measurement of the new, clean sample. After the measurement, the polymer film and masking tape were reapplied to the ortho fabric coupon. That whole assembly was attached to release paper and then stored in a Petri dish. A photo of a new sample is shown in Figure 13.



Figure 13. Ortho-Fabric Sample with Gold-Kapton Masking

4 Loading of Test Samples with Simulant

4.1 Description

4.1.1 Selection of Simulant

The BP-1 simulant was used at first, but the particle size distribution was too coarse to truly challenge the vacuum cleaner. Preliminary tests demonstrated that the remaining dust was barely visible and that the vacuum cleaner removed 100% of the BP-1 particles. The vacuum power setting was not recorded for these tests. However, it was observed that after pressing and spreading the simulant onto the Ortho fabric with the spatula, nearly all of it fell off when turned upside down and tapped lightly (a characteristic that was not previously observed in the vacuum cleaner testing in 2009). This was hypothesized to be due to a PSD that skewed towards larger particle sizes. Figure 10 illustrates the PSD shape of BP-1 compared with other lunar simulants. JSC-1A was no longer available. Subsequently, LHS-1D was chosen for testing, with Green Spar as a backup.

4.1.2 Selection of Deposition Method

The selected deposition method was intended to have several characteristics. First, the deposition needed to be homogeneous, meaning it was evenly spread throughout the entire area to be cleaned. It also needed to be representative of a real-world scenario. Lastly, it was desired to have a monolayer, if possible. This would allow for better correlation with known existing models of particle deposition.

In considering the need to represent a real-world scenario, two types of events were assumed for contaminating the Ortho fabric during an EVA. The first event involves lunar regolith being rubbed onto the fabric, as one might expect when kneeling. The second involves electrically charged dust particles being attracted to the suit due to tribocharging or other means. A powder sprayer was considered to address this second type of event. Examples of this device included a Microtrac Camsizer M1, a hand sprayer, and a modification of the hand powder sprayer.

After discussion with experts at KSC, it was concluded that accurately replicating the charged conditions would not only be complicated, difficult, and expensive, but it would most likely not represent the worst case conditions for contaminating the suit. Whereas electrostatically charged dust would settle on top of the fabric, dust that had more forceful and direct contact, such as by kneeling and rubbing, has a greater chance of penetrating through the fabric fibers. Therefore, a method was developed to simulate rubbing of the regolith onto the Ortho fabric.

To minimize loading inconsistencies due to human involvement (e.g., using a spatula to spread and rub in simulant), a simulant loading device was developed (Figure 14). With this device, the following parameters could be controlled:

- Downward force – It is expected that penetration of dust into fabric is dependent on the applied force.
- Angle of attack – An object rubbing against the lunar regolith at different angles will have different effects.
- Roundness or texture of rubbing surface – It could simulate different surfaces such as a sharp rock, rounded object, another fabric, or textured rock.

- Amount of rubbing – This was controlled by the number of cycles used to move the pull-ring back and forth.

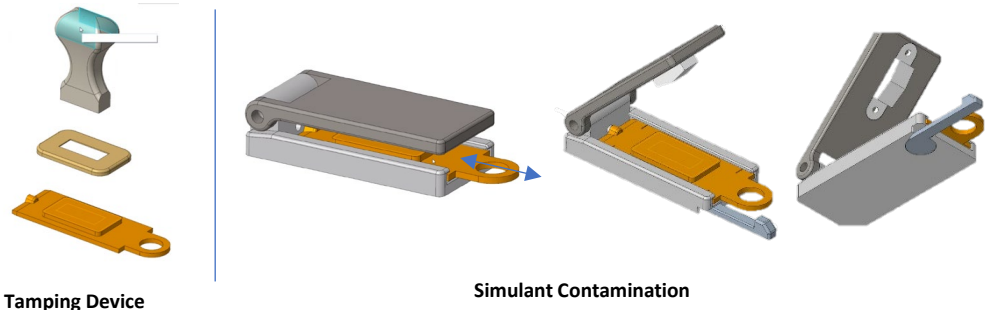


Figure 14. Simulant Loading Device (SLD)

4.2 Mitigation of Uncertainty

4.2.1 Inconsistent Loading (Distribution)

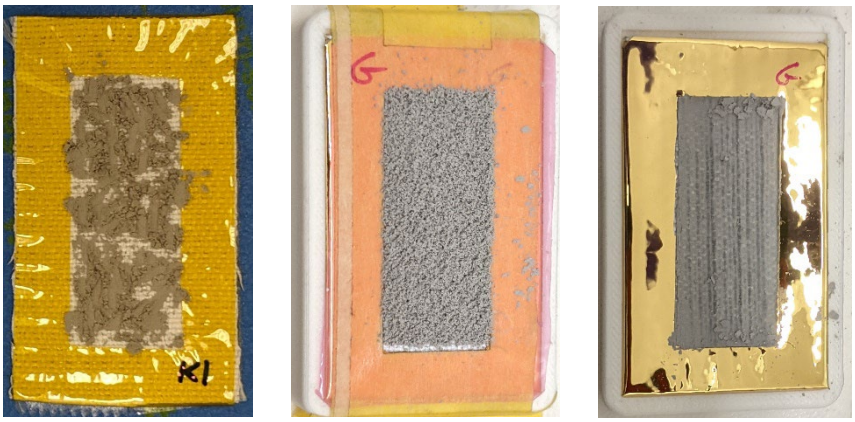
Inconsistent distribution of the loading across the area of the simulant could lead to errors. For example, if the area to be cleaned were divided into two parts, one part having 100% particulate removal efficiency and the other part having 0% particulate removal efficiency, and all of the simulant was on the side that had 0% particulate removal efficiency, then it would seem as if particulate removal efficiency of the entire surface was zero percent. Conversely, if the simulant was on the efficient side of the test coupon, it would seem as if there was 100% particulate removal efficiency. However, the particulate removal efficiency is actually 50% in this case, but this would not be observed because the distribution was not consistent across the entire sample.

In the example above, the removal efficiency is not consistent across the surface, and this would also be the case for a real-world scenario and the testing scenario. The uneven removal efficiency on the surface would be caused by uneven profile of friction velocity across the surface. Friction velocity is a way of representing shear stress at the surface that is caused by nearby air velocity. As an example, the friction velocity near the edges would be less than the velocity towards the middle.

It should be noted that by conducting multiple tests, the discrepancies caused by inconsistent loading distribution would be expected to be statistically averaged out to the correct value. However, having a consistent loading distribution for all cases would mean that a lower number of tests would be needed to average out inconsistencies. Also, if all tests were consistently not loading near the edges of the sample, as an example, then the test results would be skewed towards the performance of the interior portion of the sample and not take into account the edge effects. Therefore, trying to ensure that loading distribution is consistent throughout the entire surface, including the edges, ensures a more correct answer.

To mitigate any uncertainty caused by inconsistent load distribution, dust was applied to the fabric by brushing through a screen. Figure 15 shows the distribution results using a brush and screen versus applying and spreading with a spatula. Note that the simulant tended to coagulate, creating agglomerations which made it difficult to create a very even distribution. Brushing the

dust through the screen helped solve this problem by breaking up the agglomerations as it was deposited onto the fabric.



Splotchy Distribution (no screen) | **Even Distribution (with screen)** | **After Using Sample Loading Device (Spatula)**

Figure 15. Comparison of Loading Distribution from Different Methods

4.2.2 Inconsistent Loading (Mass/Layers)

Greater amounts of mass added to the Ortho fabric will result in a thicker layer of deposited simulant. Tests on different thicknesses of simulant will have different removal efficiencies. This is because the particles that are in direct contact with the surface are going to be the hardest to remove while the particles that are above the first layers of the simulant are going to be easily removed. This is due to the fact that the particles on the upper layers of the simulant are going to agglomerate and create larger particles that are going to be easier to remove and draw into the airstream of the vacuum. It is known that smaller particles in contact with the surface are going to be the most difficult to remove. Therefore, if the smaller particles are allowed to agglomerate into larger particles, they will be much more easily removed.

Another factor that needed to be controlled was the amount of simulant that was embedded into the fabric fibers. This simulant embedded into the fibers of the Ortho fabric would be much more difficult to remove than the particles on the surface of the fabric. Therefore, the mass of the simulant embedded in the fibers needed to be consistent amongst the test coupons.

Uncertainties due to inconsistencies in the mass, either above or below the surface of the fabric, were mitigated in two ways. First, the initial mass of the simulant deposited through the screen and onto the fabric was measured to be consistently 100 milligrams +/- 0.1 milligram. Also, by controlling the rubbing process and the number of cycles that the pull ring was operated, the amount of dust that penetrated the fibers was expected to be controlled. Additionally, the SLD was also expected to control the amount of dust swept from the surface. After use of the SLD, a brushing step was added to have additional control the top layer of dust.

The penetration depth and dust thickness layer were not measured in these tests. However, the consistency of total mass deposited was demonstrated through mass measurements, shown in Figure 16. Additionally, lunar simulant that penetrated through the fabric when using the SDL was collected onto masking tape adhered to the backside of the sample, and the mass was measured. See Figure 17.

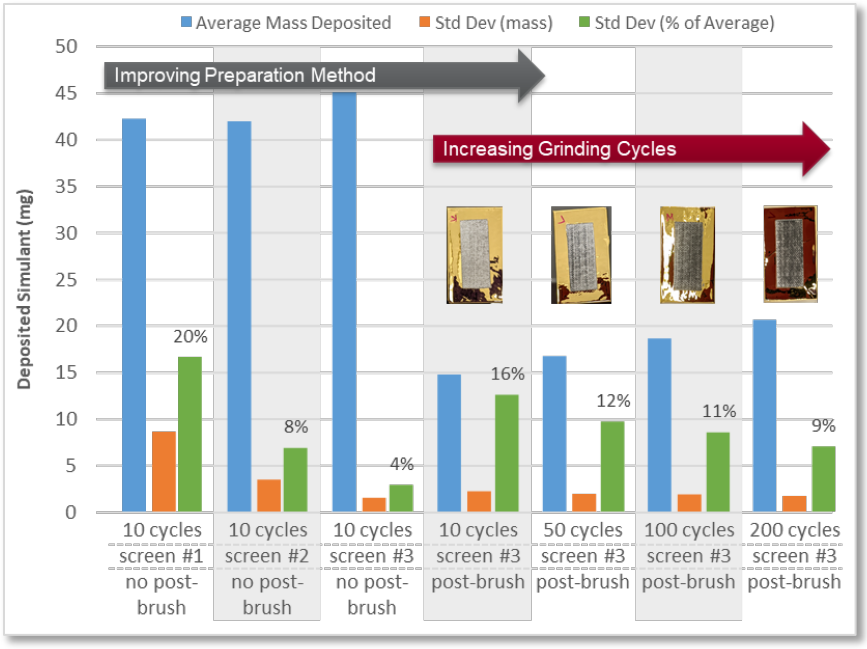


Figure 16. Simulant Deposited on Fabric Samples

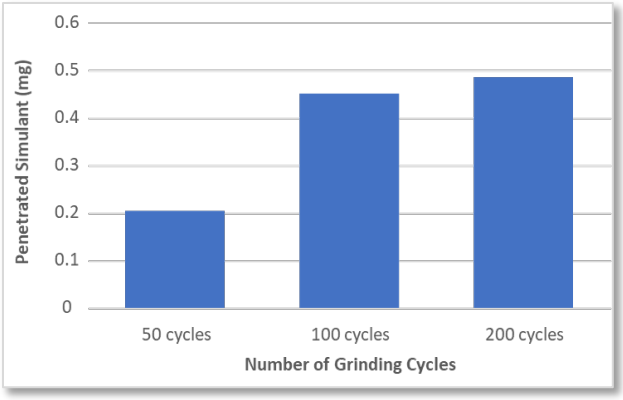


Figure 17. Dust Penetrated Through Ortho fabric

It is a hope that future testing and analysis will verify consistency of penetration depth and thickness of the dust layer and show how it changes before and after vacuum testing. Some 3D microscopy photos taken with the Keyence microscope in the Simulant Development Lab may help. These photos can show the topography with measurements of the surface.

4.2.3 Initial Adhesion and Cohesion

The initial adhesion and cohesion of the test particles affect the resulting loaded test sample and subsequently affects the percent that would be removed by the vacuum cleaner. Loosely deposited particles would have poor adhesion and cohesion. For loosely deposited particles, the simulant loading device would remove most of the particles during the sliding process, leaving very little to remove from the sample surface. Compacted particles, on the other hand, have very good adhesion and cohesion. The compacted mass of dust behaves more like a single larger mass, much like compacted fine soil or sand. The compacted simulant remains in contact with the fabric longer, allowing for better adhesion to the surface and better penetration into the fibers. Use of a tamping tool on a mass scale allows controlled and repeatable compaction of the simulant.

4.3 Procedure for Loading Samples

One hundred milligrams of dry LHS-1D simulant was measured and set aside in a Petri dish alongside the new samples that were created. The new samples were positioned in the simulant loading device, and a brush was used to evenly add the measured simulant through the screen. The screen was then removed from the sample holder and the sample holder, along with the sample, was placed on a scale. A downward force was applied with the tamping device until a reading of approximately 8,000 grams was measured. The items used for sample preparation are shown in Figure 18.



Figure 18. Sample Preparation Setup

The sample holder was inserted into the sample loading device, and the hinged top was closed. A weight of 1.41 pounds was set on top of the SLD. The pull-ring was moved back and forth for the desired number of cycles, where one movement of back-and-forth equaled one cycle. Then a paintbrush was brushed back-and-forth, twice, over the surface of the test sample. The sample holder was removed from the main body and then turned upside down, but with no tapping or sudden movement, to release any dust that had poor adhesion, particularly the dust that was moved away from the test surface and coagulated. The masking tape and polymer film were then removed to reveal the gold surface. At this time, the mass was again measured, and the loaded sample was stored in a petri dish. An example of the finished product is shown in Figure 19.

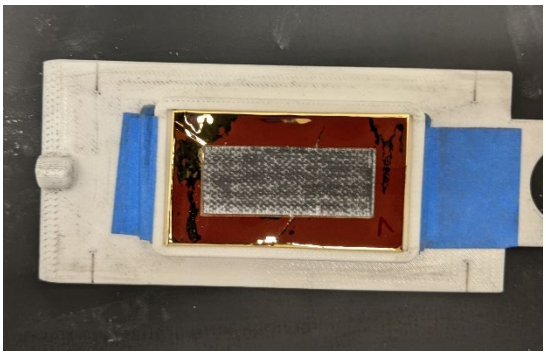


Figure 19. Finished Product (200 grinding cycles)

A total of 22 loaded samples were created. These are listed in the table below.

Table 1. Sets of Test Samples Created with the Simulant Loading Device

	Sliding Cycles	**Screen**	**Post-Brush**
A	10	#2	No
B	10	#1	No
C	10	#3	No
D	10	#3	Yes
E	50	#3	Yes
F	100	#3	Yes
G	200	#3	Yes

5 Particulate Removal by Airflow (Vacuum Cleaner Testing)

5.1 Description

Testing was performed to determine the resuspension curve (trend and removal efficiency as a function of time) for the conditions tested. The parameters expected to have significant effect on the resuspension curve are the following:

- Contamination methods and initial mass – the contamination method, including factors such as the number of cycles activating the pull ring on the SLD, was expected to influence the final results. Therefore, a trend could potentially be seen for increasing the number of rubbing cycles. Other parameters that could be varied include the initial loading amount, attack angle of the "contact slide", and roundness of the "contact slide".
- Air velocity – A higher velocity would result in a higher removal efficiency. Also, higher velocity would be required to remove smaller particles.
- Surface material – particle adhesion is highly dependent on the surface material. For example, it was noted that the lunar simulant adhered very well to paper and plastic materials while it did not adhere well to polished metal materials. This is partly due to material surface energy properties, but it is also attributed to other factors as well.
- Humidity – higher humidity results in greater particle adhesion.
- Temperature – lunar regolith particles in contact with space suit material at low temperatures may have different adhesion properties than at higher temperatures.
- Duration of contact – a longer contact time can result in higher adhesive forces between the particle and the surface. This is because the contact distance between the particle and the surface can gradually decrease due to the contact forces slowly deforming the contact surfaces over time.
- Electrostatic charging – electrostatic charging of particles and surfaces, due to various causes, can affect the overall adhesion.

Parameters affecting the contamination and two flow settings on the vacuum cleaner were varied for this set of tests, leaving other parameters that affect resuspension to be investigated in future experiments. The sets of samples included in testing are listed in Table 1. Each set used different parameters for contamination. The vacuum cleaner had three possible power settings: Eco, Med, and Boost. Two power settings, Med and Boost, were varied for the tests.

5.2 Mitigation of Uncertainty

There are various attributes from testing that could lead to uncertainty in the test results. This section identifies potential sources of uncertainty and the steps taken to mitigate their impact on results.

5.2.1 Inconsistent Vacuuming (Position)

The removal force that the airflow imparts onto the deposited particles is dependent on flow geometry. The change in position relative to the test sample would change that flow geometry. Therefore, the position of the vacuum cleaner with relation to the test coupon was controlled through the use of guiding lines that were placed on the test table.

5.2.2 Inconsistent Vacuuming (Speed)

This set of tests was conducted with the vacuum cleaner in a static condition, meaning the vacuum tool did not move in relation to the test sample.

Future tests were to have movement of the vacuum cleaner in one direction. For these tests, a video camera would have been used in conjunction with equidistant markings set up on the test bench in the path of the vacuum cleaner tool. Review of the video footage would provide a verification of the speed of the tool during testing. Another suggestion is to set up the vacuum cleaner on a motorized track so that the speed of the motor can be set electronically.

5.2.3 Inconsistent Vacuuming (Flow Rate)

The vacuum cleaner power setting was maintained constant at the medium setting for most test points to get a representative resuspension curve at a constant flow rate. Since it was known that the pressure drop across the vacuum tool directly relates to the flow rate, the pressure drop was measured for each of the tests as a verification of having consistent flow rate. A few additional test points were performed at the “Boost” setting in order to obtain data for the higher flow rate.

5.2.4 Recording of Time

The vacuum cleaner was operated by hand to obtain removal fraction as a function of time. The start and stop times of the operation of the vacuum cleaner were recorded by observing the elapsed time displayed in the data acquisition program. This hand-recorded time was used to obtain an approximate duration for each test point in testing. However, more accurate test point duration values were determined by analyzing the step changes in the pressure transducer output.

5.3 Procedure for Testing

The loaded sample was placed into testing position using the guidelines that were placed on the tabletop surface. The loaded sample was then secured to the tabletop with the securing tape. The vacuum cleaner tool was positioned over the sample using the guides provided. The vacuum cleaner was activated for a specified duration. It should be noted that the vacuum cleaner was hand operated, but the actual duration of the test point was determined by analysis of data recorded by the data acquisition program. The sample was then removed, pictures were taken, and mass was measured and recorded. This set of procedures was repeated for the remaining test durations and test samples. A picture of the test setup is shown in Figure 20. A list of the test point durations for each test sample is given in Table 2.

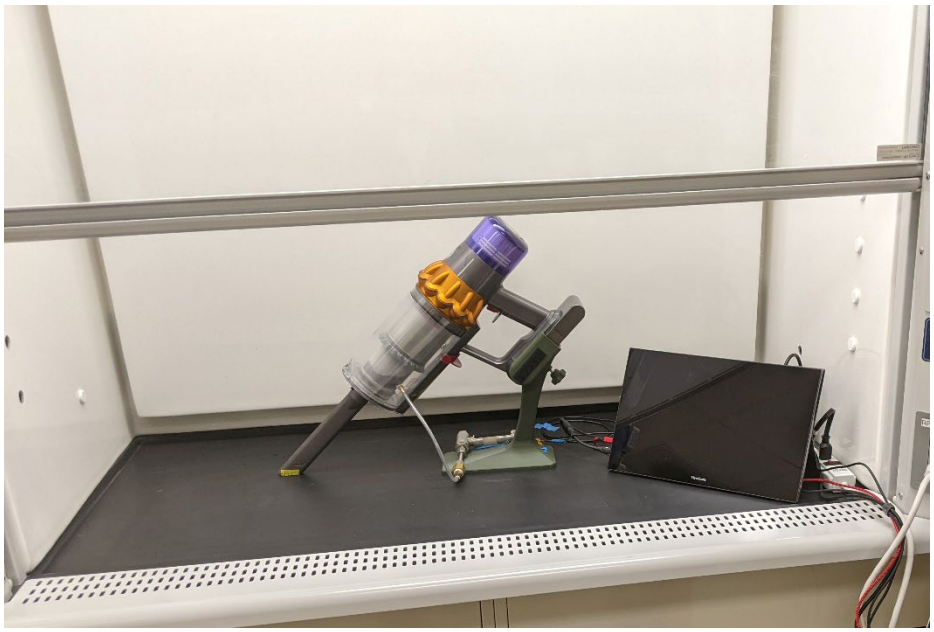


Figure 20. Vacuum Testing Setup

Table 2. Test Point Durations

Test Point Duration (seconds)	Elapsed Time (seconds)
0.5	0.5
0.5	1
4	5
10	15
15	30
90	120
180	300

5.4 Test Results

Data collected from testing was used to create the resuspension curve shown in Figure 21. A review of these curves shows that from sets A through C the uncertainty in the results decreased. Also, the maximum removal after five minutes at a medium setting was approximately 80-85%. Adding the post brush step in set D increased the uncertainty. However, this was not unexpected

because these test samples started with a smaller amount of simulant mass and more pronounced variations in the results were expected. A decrease in the total percent removed from the surface was also expected due to the fact that the most easily removed particles were already removed with the post-brushing step. The number of sliding cycles increased from set D through set G. Overall, the percentage removed seemed to increase between sets D and E, increasing from 10 cycles to 50 cycles. However, results from the two sets overlap; a greater number of test points would need to be performed to determine if there is a trend, or if the results are essentially the same. The percent removal decreased for set F, 100 cycles, and then even more for set G, 200 cycles. The uncertainty was greatly decreased for set G. So, it seems that increasing the number of sliding cycles increases the consistency of the test results.

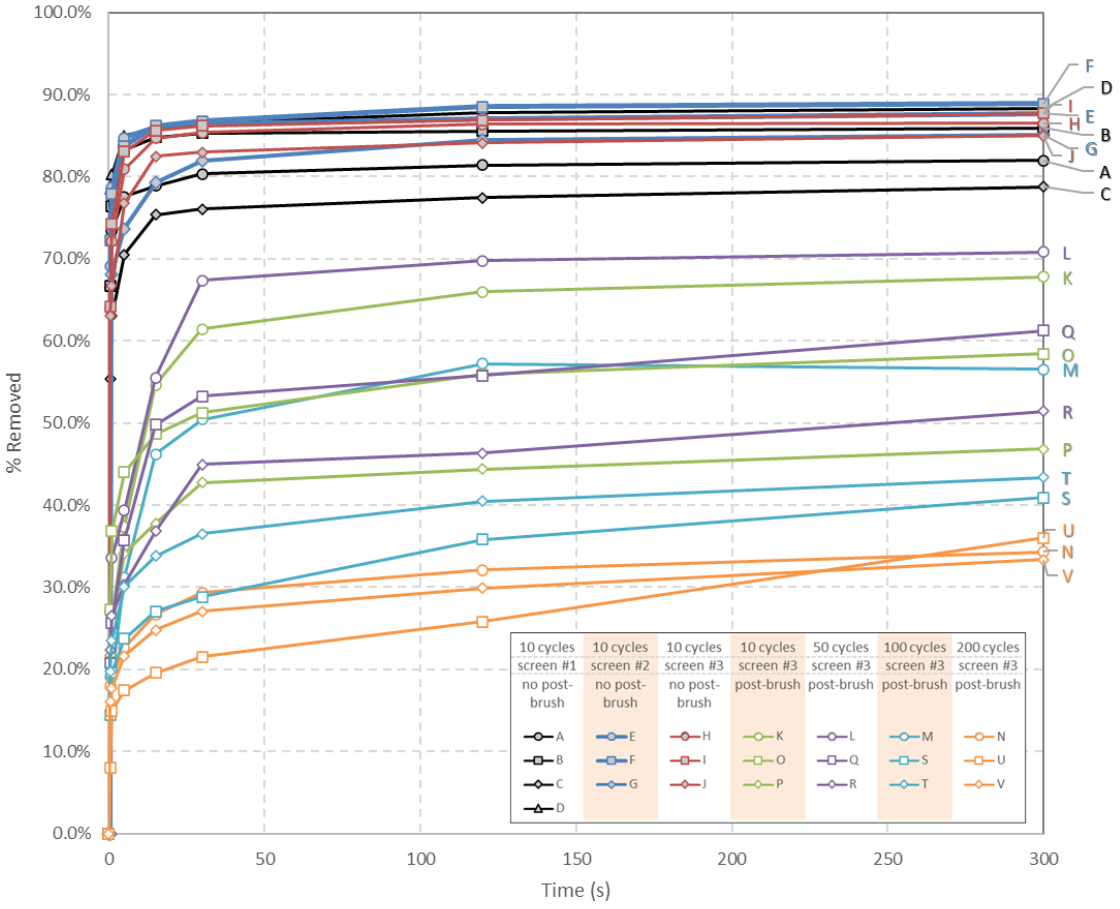


Figure 21. *Percent Simulant Removed as Function of Time*

6 Predictive Model

A particle resuspension algorithm has been implemented in Python to supplement experiments supporting the development of a lunar vacuum cleaner for use in upcoming Artemis lunar missions.

6.1 List of Symbols

a Distance between asperities

D Tube diameter (for friction velocity estimation)

f Flow friction factor

F Total aerodynamic force on a particle

F' Normalized aerodynamic force

F_a Adhesive force of perfect sphere on planar surface

F_{asp} Adhesion force at an asperity

F'_{asp} Normalized adhesive force

$F'_{asp,i}$ Discretized value of F'_{asp} at index i

$F'_{asp,max}$ Upper bound of F'_{asp} numerical integration range

$F'_{asp,min}$ Lower bound of F'_{asp} numerical integration range

$F'_{aspc,i}$ Geometric mean of $F'_{asp,i-1}$ and $F'_{asp,i}$

F_D Drag component of aerodynamic force on particle

F_L Lift component of aerodynamic force on particle

F_t Fluctuating (time-varying) component of aerodynamic force

i Index for normalized adhesive force discretization

j Index for time discretization

k Final value of time discretization index

K Flow resistance coefficient

L Tube length (for friction velocity estimation)

N_R Fraction of particles remaining

N_{RS} Fraction of particles resuspended (removed)

N_{Ro} Initial fraction of particles on surface (usually = 1)

$\Delta n_{i,k}$ Fraction of N_R within interval $\left[F'_{asp,i-1}, F'_{asp,i}\right]$ at time t_k

n_θ Forcing frequency of turbulent component of flow

p Resuspension rate constant

Δp Fluid frictional pressure drop along length of tube

$\overline{p_{i,j}}$ Arithmetic mean of resuspension rate constant at times t_{j-1} and t_j, evaluated at $F'_{aspc,i}$

r Particle geometric mean radius

t	Time
Δt_j	Time difference $t_j - t_{j-1}$
r'	Nondimensionalized particle radius
u_τ	Friction velocity of gas
V	Flow speed
X	Multiplier of logarithmic F'_{asp} standard deviation to determine integration range limits
$\langle x \rangle$	Statistical average of quantity x
$\dot{x}$	Time rate of change of quantity x
γ	Adhesive surface energy of particle on substrate
μ	Gas dynamic viscosity
ν	Gas kinematic viscosity
ρ	Gas density
${\sigma_a}'$	Adhesive spread factor
τ	Fluid shear stress
τ_{adh}	Adhesion moment
τ_{aero}	Aerodynamic moment about point *P*
φ	Probability density of normalized adhesive force

6.2 Rock'n'Roll Resuspension Model ([RH], [Biasi], [Vincent])

The Biasi, et. al. (2001) implementation of the "Rock'n'Roll" model by Reeks and Hall, as further documented by Vincent, et. al. (2019), was selected for implementation. The Rock'n'Roll model assumes that each particle is fully resuspended from a surface if the aerodynamic moment on the particle is sufficient to roll the particle off one of the points of adhesion.

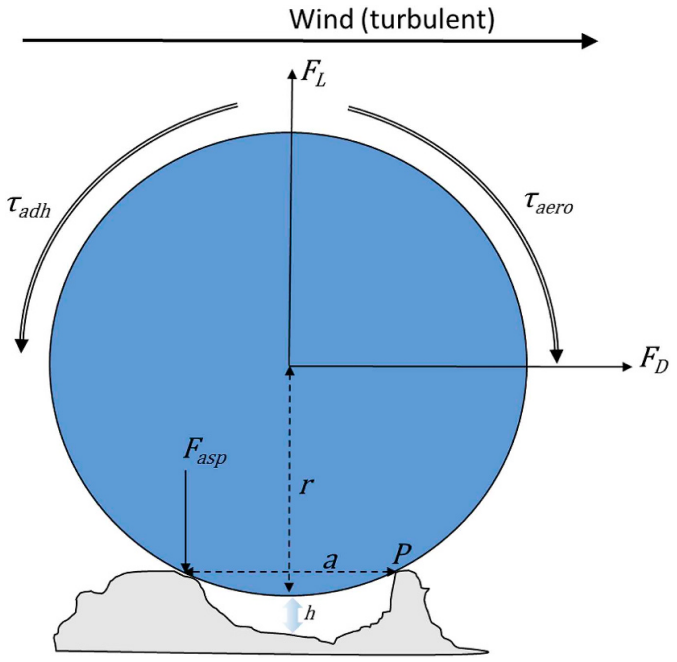


Figure 22. Moment balance for rolling resuspension model (reproduced from Vincent et. al. 2019)

Though the original implementation of the model considered dynamic effects and resonance, these effects were observed to have minimal effect on the resuspension results (Biasi et. al., 2001). Therefore, the selected model is based on a quasi-static force balance, in which the particle is resuspended if the aerodynamic moment τ_{aero} is greater than the adhesion moment τ_{adh} about point *P*. Assuming a distance a between pivot point *P* and the point of application of adhesion force F_{asp}, the adhesion moment is

$$\tau_{adh} = a \cdot F_{asp} \quad (1)$$

Similarly, the total aerodynamic moment about *P,* produced by the lift force F_L and drag force F_D, is

$$\tau_{aero} = \frac{a}{2} \cdot F_L + r \cdot F_D \equiv a \cdot F \quad (2)$$

The aerodynamic removal force F is defined as the ratio of the total aerodynamic moment τ_{aero} to the asperity-to-pivot distance a. The particle is resuspended when the following conditions applies:

$$F = \frac{1}{2} \cdot F_L + \frac{r}{a} \cdot F_D > F_{asp} \quad (3)$$

The force condition of equation 3 is used to statistically determine resuspension rate constant p, which is defined such that

$$\frac{dN_R}{dt} = -pN_R \quad (4)$$

where N_R is the fraction of particles remaining on the surface.

Solving equation 4 for N_R yields

$$N_R = N_{Ro} \exp\left(-\int_0^t p dt \right) \tag{5}$$

If N_{Ro}, the fraction of particles remaining at initial time $t = 0$, equals 1, equation 5 becomes

$$N_R = \exp\left(-\int_0^t p dt \right) \tag{6}$$

The aerodynamic removal force F is driven by turbulent fluctuations and is characterized by an average $\langle F \rangle$ and a fluctuating component F_t as follows:

$$F = \langle F \rangle + F_t \tag{7}$$

By definition, the mean of the fluctuating component F_t of aerodynamic removal force F is zero. Based on equations 3 and 7, the point of particle detachment thus occurs when $F_t = F_{asp} - \langle F \rangle$.

Reeks and Hall (Biasi et. al., 2001) derive the following expression for rate constant p under the assumptions that both F_t and its first order time derivative $\dot{F}_t$ are statistically independent of each other and that they are both Gaussian random variables:

$$p = \begin{cases} n_\theta & \dfrac{F_{asp} - \langle F \rangle}{\sqrt{\langle F_t^2 \rangle}} \le 0.75 \\ n_\theta \exp\left[-\dfrac{\left(F_{asp} - \langle F \rangle \right)^2}{2\langle F_t^2 \rangle} \right] \Bigg/ \dfrac{1}{2}\left\{ 1 + \operatorname{erf}\left[\dfrac{F_{asp} - \langle F \rangle}{\sqrt{2\langle F_t^2 \rangle}} \right] \right\} & \dfrac{F_{asp} - \langle F \rangle}{\sqrt{\langle F_t^2 \rangle}} > 0.75 \end{cases} \tag{8}$$

where n_θ is the forcing frequency of the flow's turbulent component, as defined by

$$n_\theta \equiv \frac{1}{2\pi} \sqrt{\frac{\langle \dot{F}_t^{\,2} \rangle}{\langle F_t^2 \rangle}} \tag{9}$$

The turbulent forcing frequency n_θ is also the maximum resuspension rate when resonant energy transfer is negligible. Thus, for inputs that cause the value of the lower expression on the right side of equation 8 to exceed n_θ, which occurs when $\left(F_{asp} - \langle F \rangle \right) / \sqrt{\langle F_t^2 \rangle} \lesssim 0.75$ (actually 0.729), the value of p is limited to n_θ, as indicated by equation 8.

The aerodynamic force F is a combination of lift and drag forces F_L and F_D, as shown in equation 3. The following mean lift force $\langle F_L \rangle$ correlation was suggested by Reeks and Hall

(2001), based on earlier measurements by Hall, and utilized by subsequent implementations of the Rock'n'Roll model:

$$\frac{\langle F_L \rangle}{\rho \nu^2} \approx 20.9 \left(\frac{r u_\tau}{\nu}\right)^{2.31} \quad 10$$

where ρ and ν are the gas density and kinematic viscosity, r is the mean particle radius, and u_τ is the friction (shear) velocity. Reeks and Hall (2001) suggested a correlation for mean drag force by noting that the mean drag on a sphere near a surface in simple shear flow is 1.7 times the Stokes drag [O'Neil, 1968], producing the following estimate of mean drag:

$$\frac{\langle F_D \rangle}{\rho \nu^2} \approx 32 \left(\frac{r u_\tau}{\nu}\right)^{2} \quad 11$$

Equations 3, 10, and 11 combine to provide the following expression for mean aerodynamic force

$$\frac{\langle F \rangle}{\rho \nu^2} = \frac{1}{2} \cdot \frac{\langle F_L \rangle}{\rho \nu^2} + \frac{r}{a} \cdot \frac{\langle F_D \rangle}{\rho \nu^2} = \frac{1}{2} \cdot 20.9 \left(\frac{r u_\tau}{\nu}\right)^{2.31} + \frac{r}{a} \cdot 32 \left(\frac{r u_\tau}{\nu}\right)^{2} \quad 12$$

The particle radius-to-asperity distance ratio, known as the geometric factor $G_f \equiv r/a$, is obtainable from the ratio of tangential-to-normal force required to dislodge identical particles from a surface, as determined using a centrifuge. Biasi et. al., 2001 suggested a G_f of approximately 100, based on measurement results. Thus, the mean aerodynamic force of equation 12 reduces to

$$\frac{\langle F \rangle}{\rho \nu^2} = 10.45[r'^{2.31} + 306 r'^{2}] \quad 13$$

where

$$r' \equiv \frac{r u_\tau}{\nu} \quad 14$$

The ratio of root-mean-squared-to-mean lift is 0.2, as suggested by Hall (1998) and Biasi et. al., 2001. This ratio is also assumed applicable for drag, in the absence of drag-specific data. Therefore, the 0.2 root-mean-squared-to-mean-lift ratio also applies to total aerodynamic force F since it is a linear combination of lift and drag forces, in accordance with equation 3:

$$\frac{\sqrt{\langle F_t^2 \rangle}}{\langle F \rangle} \approx 0.2 \quad 15$$

The turbulent forcing frequency n_θ, derived from Hall's lift force energy spectrum measurements and assumed applicable to the effective fluctuating force F_t, is

$$n_\theta = 0.00658\left(\frac{u_\tau^2}{\nu}\right) \tag{16}$$

The adhesion force F_{asp} is a random quantity, even in cases of monodisperse particle sizes. The variability of the random adhesion force is reduced by normalization with respect to the adhesion force of a sphere of radius r in contact with a perfectly smooth surface, which is given by Johnson, Kendall, and Roberts as

$$F_a = \frac{3}{2}\pi\gamma r \tag{17}$$

where γ is the adhesive surface energy of the particle-substrate combination. Some known surface energies γ are:

- Graphite on stainless steel: 0.15 J/m^2
- Alumina on stainless steel: 0.56 J/m^2

If the adhesive force F_{asp} is proportional to particle radius r, normalizing F_{asp} by F_a

$$F'_{asp} \equiv \frac{F_{asp}}{F_a} \tag{18}$$

removes the radius-dependence of the scaled result. he normalized adhesion force is assumed to have a lognormal probability density:

$$\varphi\left(F'_{asp}\right) = \frac{1}{\sqrt{2\pi}}\left(\frac{1}{F'_{asp}\ln{\sigma_a}'}\right)\exp\left\{-\frac{1}{2}\left[\frac{\ln\left(\frac{F'_{asp}}{\langle {F_{asp}}'\rangle}\right)}{\ln{\sigma_a}'}\right]^2\right\} \tag{19}$$

where $\langle {F_{asp}}'\rangle$ is the geometric mean of F'_{asp} and ${\sigma_a}'$ is the adhesive spread factor. The quantity $1/\langle {F_{asp}}'\rangle$ is called the adhesive reduction factor. Whereas these factors were experimentally determined by Reeks and Hall for specific instances alumina and graphite particles on polished stainless steel, Biasi, et. al. (2001) developed the following correlations by combining the results from four previous experimental investigations (including those of [RH]) for particles ranging in diameter from 0.1 μm to 30 μm:

$$\langle F'_{asp}\rangle = 0.016 - 0.0023r^{0.545} \tag{20}$$

$$\sigma'_a = 1.8 + 0.136r^{1.4} \tag{21}$$

These correlations were also used by Vincent, et. al. (2019).

Substituting equation 18 into equation 8 yields the following expression of rate constant p as a function of normalized force parameters:

$$p = \begin{cases} n_\theta & \dfrac{F'_{asp} - \langle F' \rangle}{\sqrt{\langle F_t'^2 \rangle}} \leq 0.75 \\ n_\theta \exp\left[-\dfrac{\left(F'_{asp} - \langle F' \rangle\right)^2}{2\langle F_t'^2 \rangle} \right] \Bigg/ \dfrac{1}{2}\left\{ 1 + \operatorname{erf}\left[\dfrac{F'_{asp} - \langle F' \rangle}{\sqrt{2\langle F_t'^2 \rangle}} \right] \right\} & \dfrac{F'_{asp} - \langle F' \rangle}{\sqrt{\langle F_t'^2 \rangle}} > 0.75 \end{cases} \quad (22)$$

where

$$F' \equiv \frac{F}{F_a} = \frac{2F}{3\pi\gamma r} \quad (23)$$

and

$$F'_t \equiv \frac{F_t}{F_a} = \frac{2F_t}{3\pi\gamma r} \quad (24)$$

Combining equation 23 with equation 13 produces the following expression for mean normalized aerodynamic force:

$$\langle F' \rangle = \frac{2}{3\pi\gamma r} 10.45\rho\nu^2 [r'^{2.31} + 306r'^2] = \frac{20.9u_\tau\mu}{3\pi\gamma} [r'^{1.31} + 306r'] \quad (25)$$

Using equation 15, the root-mean-square fluctuation of the time-varying component of the aerodynamic force is

$$\sigma_t \equiv \sqrt{\langle F_t'^2 \rangle} \approx 0.2\langle F' \rangle \quad (26)$$

For a system of deposited particles whose normalized adhesion forces are distributed according to the probability density function $\varphi\left(F'_{asp}\right)$ of equation 19, the total fraction of remaining particles becomes:

$$N_R = \int_0^\infty \varphi\left(F'_{asp}\right) \exp\left(-\int_0^t p\,dt \right) dF'_{asp} \quad (27)$$

Since particles either remain or are resuspended, the fraction of resuspended particles is

$$N_{RS} = 1 - N_R \tag{28}$$

6.3 Numerical Algorithm

The current analysis assumes that the following variables and parameters are constant with respect to time:

- Surface Adhesion Energy γ
- Gas density ρ
- Gas kinematic viscosity ν
- Geometric mean particle radius r

In cases where friction velocity u_τ varies with time, the integrals in equation 27 are numerically determined using finite difference summations, providing the following approximation of remaining particle fraction $N_{R,k}$ at time t_k:

$$N_{R,k} = \int_0^\infty \varphi\left(F'_{asp}\right) \exp\left(-\int_0^t p dt\right) dF'_{asp} \approx \sum_{i=1}^{N} \left\{ \varphi_i \Delta F'_{asp,i} \exp\left[-\sum_{j=1}^{k} \overline{p_{i,j}} \Delta t_j\right]\right\} \tag{29}$$

where

$$\Delta t_j \equiv t_j - t_{j-1} \quad (j = 1, \ldots, k) \tag{30}$$

and

$$\overline{p_{i,j}} \equiv \frac{p_{i,j} + p_{i,j-1}}{2} \tag{31}$$

Additionally, φ_i is the normalized adhesion force probability density function from equation 19 and $p_{i,j-1}$ and $p_{i,j}$ are the resuspension rate constants at times t_{j-1} and t_j, which are all evaluated at an appropriate average F'_{asp} within each $\Delta F'_{asp,i}$ interval, which is designated as $F'_{aspc,i}$.

In numerically evaluating integrals with respect to F'_{asp}, the range is logarithmically discretized since the variations of the integrand mostly happen at the lower end of the range due to the lognormal nature of φ. The discretization boundaries are thus distributed according to

$$F'_{asp,i} = \exp\left\{\ln\left(F'_{asp,min}\right) + \frac{i}{N} \cdot \left[\ln\left(F'_{asp,max}\right) - \ln\left(F'_{asp,min}\right)\right]\right\} \quad (i = 0, \ldots, N) \tag{32}$$

where N is the number of intervals and $F'_{asp,min}$ and $F'_{asp,max}$ are the respective minimum and maximum boundaries of F'_{asp}. The interval differences are determined as

$$\Delta F'_{asp,i} = F'_{asp,i} - F'_{asp,i-1} \quad (i = 1, \ldots, N) \tag{33}$$

The integrand within each interval is evaluated at adhesion force values $F'_{aspc,i}$ that are arithmetic means of the interval boundaries within in the logarithmic domain:

$$F'_{aspc,i} = \exp\left\{\frac{\ln(F'_{asp,i-1}) + \ln\left(F'_{asp,i}\right)}{2}\right\} \quad (i = 1, \dots, N) \tag{34}$$

or, using equation 32:

$$F'_{aspc,i} = \exp\left\{\ln\left(F'_{asp,min}\right) + \frac{2i-1}{2N} \cdot \left[\ln\left(F'_{asp,max}\right) - \ln\left(F'_{asp,min}\right)\right]\right\} \quad (i = 1, \dots, N) \tag{35}$$

Both the lower and upper limits of the integration over F'_{asp} in equation 27 are problematic when numerically approximating the integral: the lower limit of 0 causes a singularity in the lognormal probability density $\varphi\left(F'_{asp}\right)$ (equation 19) and the upper limit of ∞ is not numerically achievable. Fortunately, the integrand value is negligibly small for all but a specific range of F'_{asp}, so the limits of the numerical integration only need to encompass the F'_{asp} values the produce integrand values of significant magnitude to affect the integrated result. This range is best determined by noting that the lognormal distribution in equation 19 is simply a Gaussian probability density function in logarithmic space with a mean of $\ln\left(\langle F_{asp}{}'\rangle\right)$ and a standard deviation of $\ln(\sigma_a{}')$. Thus, the logarithmic-space peak occurs at $\ln\left(\langle F_{asp}{}'\rangle\right)$, with the value consistently and symmetrically decreasing at $F'_{asp} = \pm X \cdot \ln(\sigma'_a)$, where X is an input that would typically be greater than 1. Thus, suitable minimum and maximum limits are given by

$$\ln\left(F'_{asp,min}\right) \equiv \ln\left(\langle F'_{asp}\rangle\right) - X \cdot \ln(\sigma'_a) \tag{36}$$

and

$$\ln\left(F'_{asp,max}\right) \equiv \ln\left(\langle F'_{asp}\rangle\right) + X \cdot \ln(\sigma'_a) \tag{37}$$

The model results shown in this document use an X value of 4.

The form of the summation approximations in equation 29 is inefficient in that the summation over time inside the exponential needs to be reevaluated for each F'_{asp} increment for each evaluation time t_k. If the time progression of N_R is to be calculated, improved computational efficiency can be achieved by noting that the exponential of a summation equals the product of the exponentials of each summand. Applying this principle to equation 29 yields

$$N_{R,k} \approx \sum_{i=1}^{N} \Delta n_{i,k} \tag{38}$$

where

$$\Delta n_{i,k} \equiv \varphi_i \Delta F'_{asp,i} \prod_{j=1}^{k} \exp\left[-\overline{p_{\iota,J}} \Delta t_j\right] \quad 39$$

By separating the k^{th} factor out of the product, a recursive formula for $\Delta n_{i,k}$ is found:

$$\Delta n_{i,k} = \varphi_i \Delta F'_{asp,i} \exp\left[-\overline{p_{\iota,k}} \Delta t_k\right] \prod_{j=1}^{k-1} \exp\left[-\overline{p_{\iota,J}} \Delta t_j\right] = \Delta n_{i,k-1} \exp\left[-\overline{p_{\iota,k}} \Delta t_k\right] \quad 40$$

Thus, the following basic algorithm is used for calculating the time profile of the fraction of remaining particles:

1. Calculate $\Delta n_{i,0}$

$$\Delta n_{i,0} = \varphi_i \Delta F'_{asp,i} \ \ (i = 1, \dots, N) \quad 41$$

2. Sum the $\Delta n_{i,0}$ to determine the initial value of $N_R = N_{R,0}$ at time t_o:

$$N_{R,0} = \sum_{i=1}^{N} \Delta n_{i,0} = 1 \quad 42$$

3. Increment the various $\Delta n_{i,0}$ to determine $\Delta n_{i,1}$ in accordance with equation 40:

$$\Delta n_{i,1} = \Delta n_{i,0} \exp\left[-\overline{p_{\iota,1}} \Delta t_1\right] \quad 43$$

4. Sum the $\Delta n_{i,1}$ to determine the initial value of $N_R = N_{R,1}$ at time t_1:

$$N_{R,1} = \sum_{i=1}^{N} \Delta n_{i,1} \quad 44$$

5. Repeat steps 3 and 4 for each successive time t_k:

$$\Delta n_{i,k} = \Delta n_{i,k-1} \exp\left[-\overline{p_{\iota,k}} \Delta t_k\right] \quad 45$$

$$N_{R,k} = \sum_{i=1}^{N} \Delta n_{i,k} \quad 46$$

Under the special case in which friction velocity u_τ is constant, the resuspension rate p is time-invariant, which simplifies equation 27 to:

$$N_R = \int_0^\infty \varphi\left(F'_{asp}\right) \exp(-p \cdot t)\, dF'_{asp} \quad 47$$

This integral is evaluated via the following discretization

$$N_R = \sum_{i=1}^{N} \varphi_i \exp[-p_i \cdot t]\, \Delta F'_{asp,i} \quad 48$$

where $t \equiv t_k - t_0$. The form in equation 48 is particularly useful for examining the effects of parameters on N_R or N_{RS} at a particular time, as long as friction velocity u_τ and the other parameters determining rate constant p are constant with respect to time. If p varies with time, the recursive algorithm should be used.

6.4 Friction Velocity

The friction velocity u_τ is a dimensionless measurement of the shear stress exerted by a flow on a surface, as given by the following relationship:

$$u_\tau \equiv \sqrt{\frac{\tau}{\rho}} \quad 49$$

Where τ is the shear stress and ρ is the fluid density.

An estimate of friction velocity can be determined in some cases using published pressure drop coefficient data. Generally, fluid pressure drop Δp is related to flow speed V via the relationship

$$\Delta p = \frac{1}{2} K \rho V^2 \quad 50$$

where, for flow through a straight pipe of length L and diameter D

$$K = f \frac{L}{D} \quad 51$$

A force balance on a tube of length L and diameter D provides a relationship between sheer stress τ and pressure drop Δp:

$$\pi D L \tau = \pi \left(\frac{D}{2}\right)^2 \Delta P \quad 52$$

Combining equations 49 through 52 yields the following expression for friction velocity:

$$u_\tau = \sqrt{\frac{f}{8}} V \qquad 53$$

6.5 Model Notes

The resuspension model was primarily developed using Python 3.7 within PyCharm 2019.2.3. Several variations of the model were implemented:

- Resuspension.py – calculates the time-varying fraction of remaining particles, utilizing a time-varying friction velocity tabular input.
    - Input file: Resuspension-input.xlsx
    - Output file: output.xlsx
- Resuspension-fn.py – reorganizes the code from Resuspension.py into functions and provides an implementation in which multiple friction velocity inputs are assumed constant with respect to time.
    - Input file: Resuspension-input-Vf.xlsx
    - Output file: Resuspension-fvel-output.xlsx
- Resuspension-P.py – adapts the code from Resuspension-fn.py to assess the pressure-dependence of the fractions of resuspended and remaining particles.
    - Input file: Resuspension-input-P.xlsx
    - Output file: Resuspension-P-output.xlsx

The Python models all depend on Numpy, pandas, Matplotlib, and the Python math library. These models each read inputs from a corresponding Excel file and output the calculated results to another Excel file.

A secondary resuspension model, Resuspension.xmcd, was developed in Mathcad for use as a check against the Python model results. The Mathcad resuspension model assumes that the friction velocity does not vary with time, apart from an initial step increase from 0 m/s to a set value. This model calculates the remaining and resuspended particle fractions at a single time, the value of which can be modified as an input.

6.6 Comparison of Model Results with Published Rock'n'Roll Model Output

To verify the Python implementation of the resuspension model, the model output was compared with published output data from [Reeks and Hall], [Biasi], and [Vincent], all of which utilize the Rock'n'Roll model from [Reeks and Hall].

Figure 23 through Figure 25 compare the results of the current Python model with the original model results reported by Reeks and Hall [Reeks and Hall] for alumina and graphite particles deposited on a polished stainless-steel surface. The plots represent the friction velocity dependence of the fraction of particles remaining on a polished stainless-steel surface 1 second after exposure to a constant-friction-velocity flow. Figure 23 and Figure 24 show respective resuspension results for 10 μm and 20 μm diameter alumina. Figure 25 shows results for

graphite. Reeks and Hall specified all of their model inputs, including mean particle diameters, adhesive reduction factors, adhesive spread factors, and adhesive surface energies. As demonstrated by comparing the "New (RH Table 4)" curves with the "Reeks and Hall" curves in all three figures, the Reeks and Hall model outputs are accurately reproduced by the Python model used in the current investigation. When the Reeks-and-Hall-specified reduction and spread values are replaced by values computed using the correlations from Biasi, et al. (2001) [Biasi] (equations 20 and 21) the resulting model results deviate significantly from the Reeks and Hall results. Though the Biasi correlations were based on multiple experimental results, including those from Reeks and Hall, the comparisons demonstrate that the correlation output can produce significant deviations for individual cases.

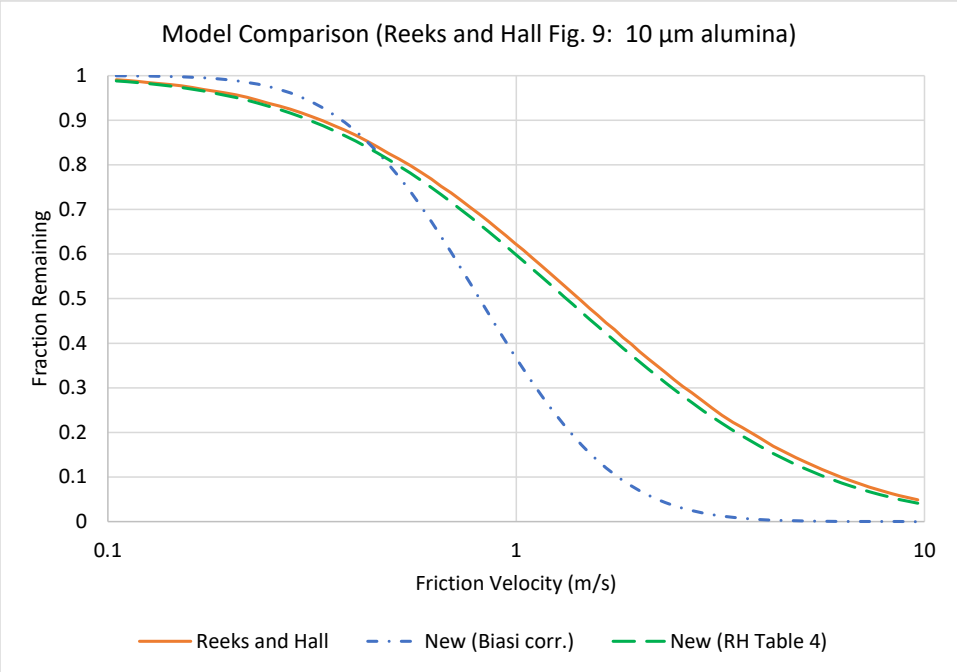


Figure 23. Comparison of Python model output with Reeks and Hall model results for fraction of remaining 10 µm diameter alumina particles on a polished stainless steel surface after 1 second of exposure to a constant friction velocity flow. "New (RH Table 4)" uses input adhesion parameters from Table 4 of Biasi et. al., 2001. "New (Biasi corr.)" uses input adhesion parameters via application of a correlation from Biasi, et al. (2001).

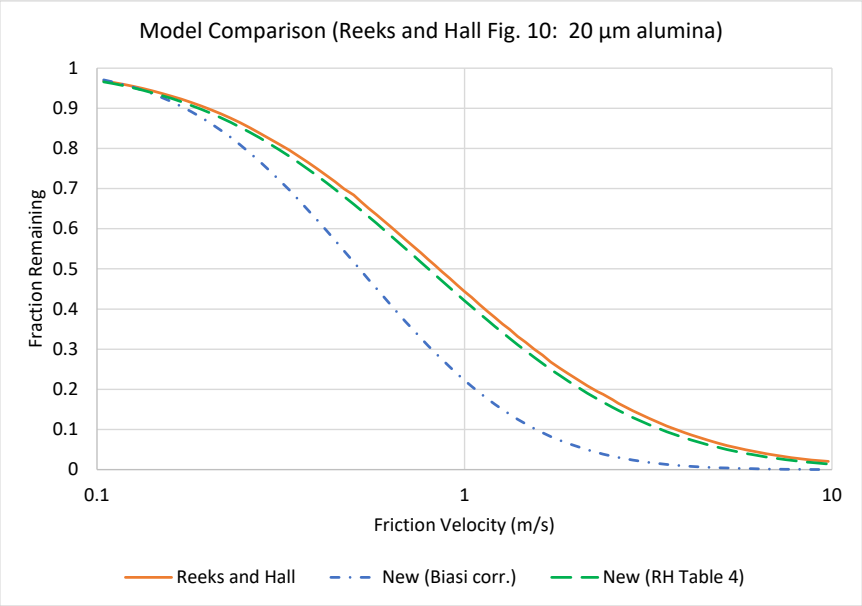


Figure 24. Comparison of Python model output with Reeks and Hall [RH] model results for fraction of remaining 20 µm diameter alumina particles on a polished stainless steel surface after 1 second of exposure to a constant friction velocity flow. "New (RH Table 4)" uses input adhesion parameters from Table 4 of [RH]. "New (Biasi corr.)" uses input adhesion parameters via application of a correlation from Biasi, et al. (2001) [Biasi].

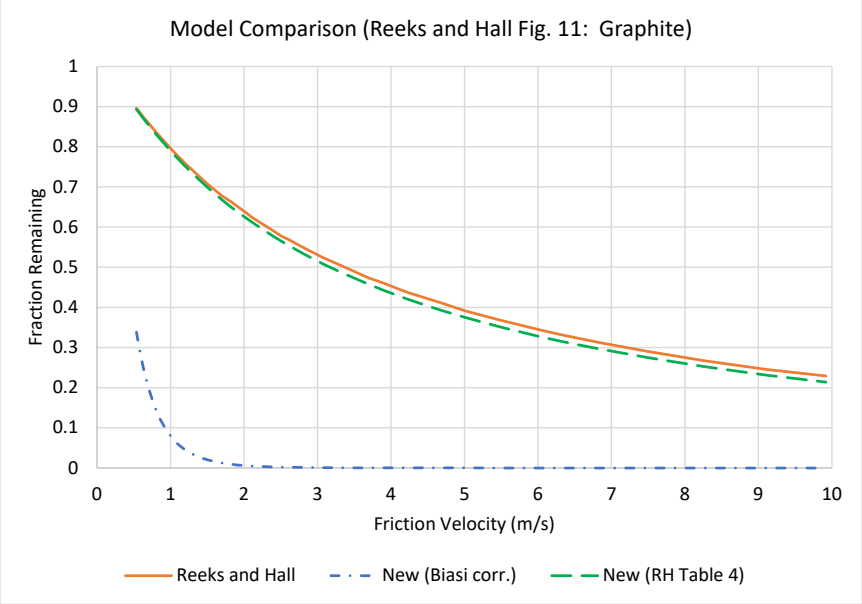


Figure 25. Comparison of Python model output with Reeks and Hall [RH] model results for fraction of remaining 13 µm diameter graphite particles on a polished stainless steel surface after 1 second of exposure to a constant friction velocity flow. "New (RH Table 4)" uses input adhesion parameters from Table 4 of [RH]. "New (Biasi corr.)" uses input adhesion parameters via application of a correlation from Biasi, et al. (2019) [Biasi].

Comparisons between the current Python model and the model results from Biasi, et al. (2001) [Biasi] appear in Figure 26 through Figure 30. Figure 26 and Figure 27 both show comparisons for graphite particles on a stainless steel surface. A surface adhesion energy of 0.15 J/m^2 was

used to generate the Python model results of Figure 26, in accordance with the value stated in Biasi et. al. (2001); however, the resulting resuspended fractions are notably higher than the results from Biasi for friction velocities less than 3.5 m/s. When using a surface adhesion energy of 0.56 J/m^2, which is used as a default value when the actual adhesion energy is unknown, the Python model results match the Biasi results extremely well, as shown in Figure 27, suggesting that Biasi used the default 0.56 J/m^2 adhesion energy for the graphite resuspension calculation.

Figure 28 exhibits a similarly excellent agreement between the Python and Biasi results for the resuspension of 20 µm alumina particles from a stainless steel surface, using an adhesion energy of 0.56 J/m^2.

Figure 29 compares the Biasi and Python results for 30 µm diameter glass microballoons resuspended from a glass surface. Since the surface adhesion energy is unknown, the 0.56 J/m^2 default is used for the Python calculation. The new Python result exhibits similar trends as the Biasi result, but the newly generated resuspended fraction is consistently approximately less than the Biasi result by approximately 0.02.

Much more significant deviations from Biasi model results are shown in Figure 30, which compares resuspension results for deposited metallic zinc particles. Since many of the other cases with well-documented inputs exhibit close matches, the deviations in Figure 30 are most likely a result of input assumptions, since quantities such as adhesion energy are not documented in the reference.

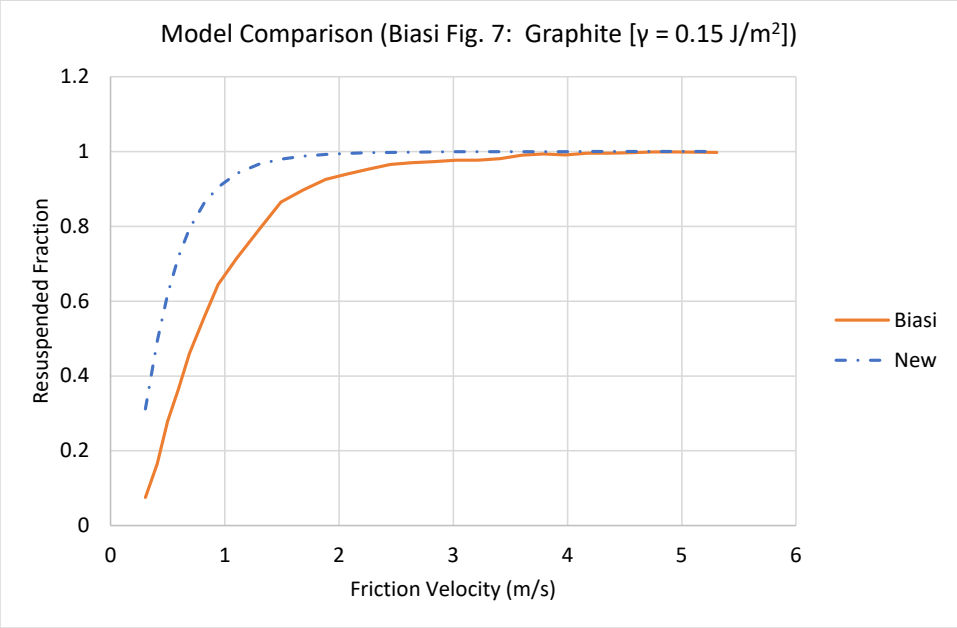


Figure 26. Comparison of Python model output with Biasi, et al. (2001) model results for fraction of graphite particles resuspended from a polished stainless steel surface by 1 second of exposure to a constant friction velocity flow, assuming a surface adhesion energy of 0.15 J/m^2.

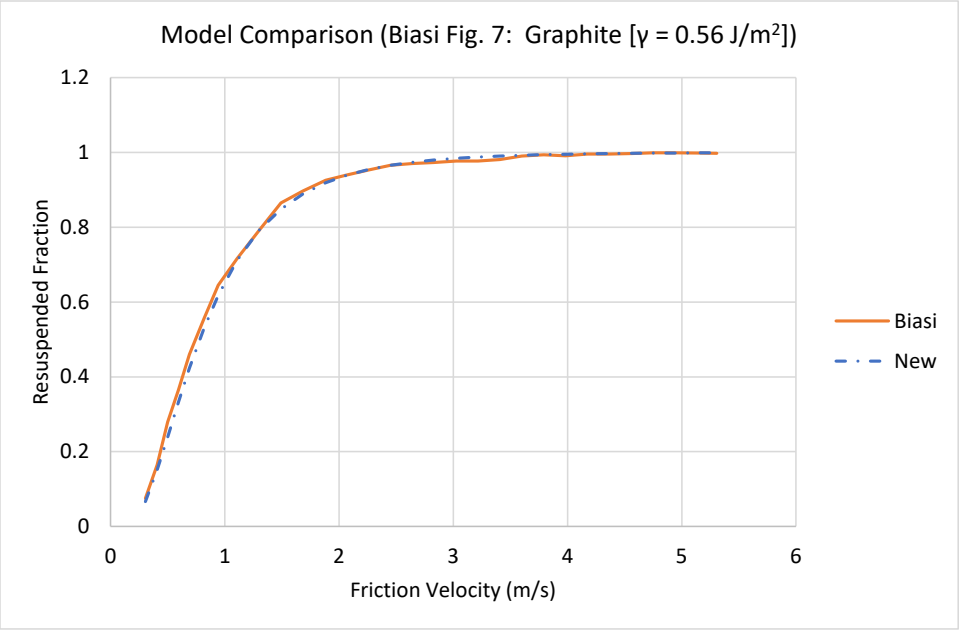


Figure 27. Comparison of Python model output with Biasi, et al. (2001) model results for fraction of graphite particles resuspended from a polished stainless steel surface by 1 second of exposure to a constant friction velocity flow, assuming a surface adhesion energy of 0.56 J/m².

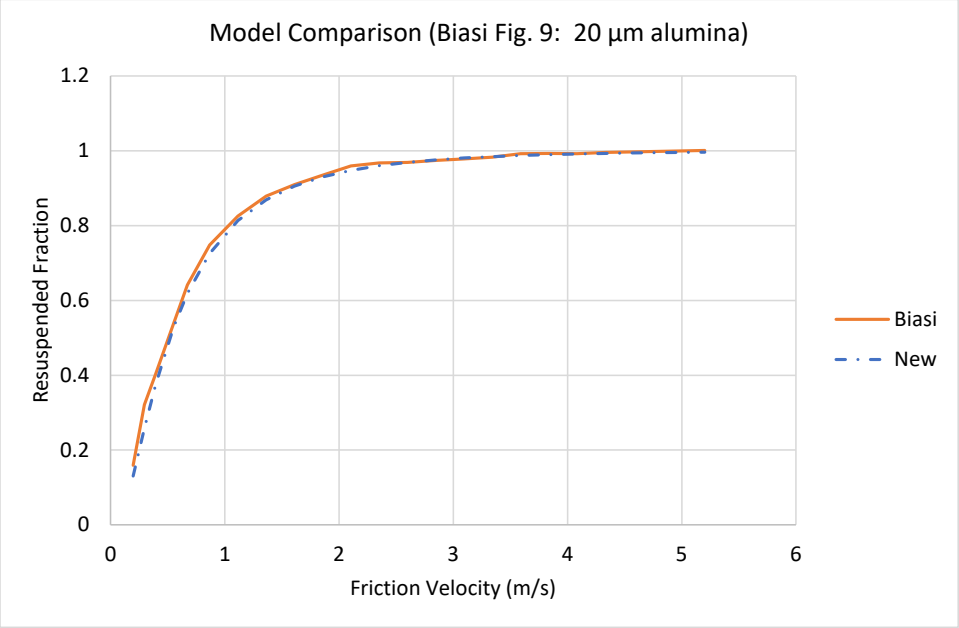


Figure 28. Comparison of Python model output with Biasi, et al. (2001) model results for fraction of 20 µm diameter alumina particles resuspended from a polished stainless steel surface by 1 second of exposure to a constant friction velocity flow, assuming a surface adhesion energy of 0.56 J/m².

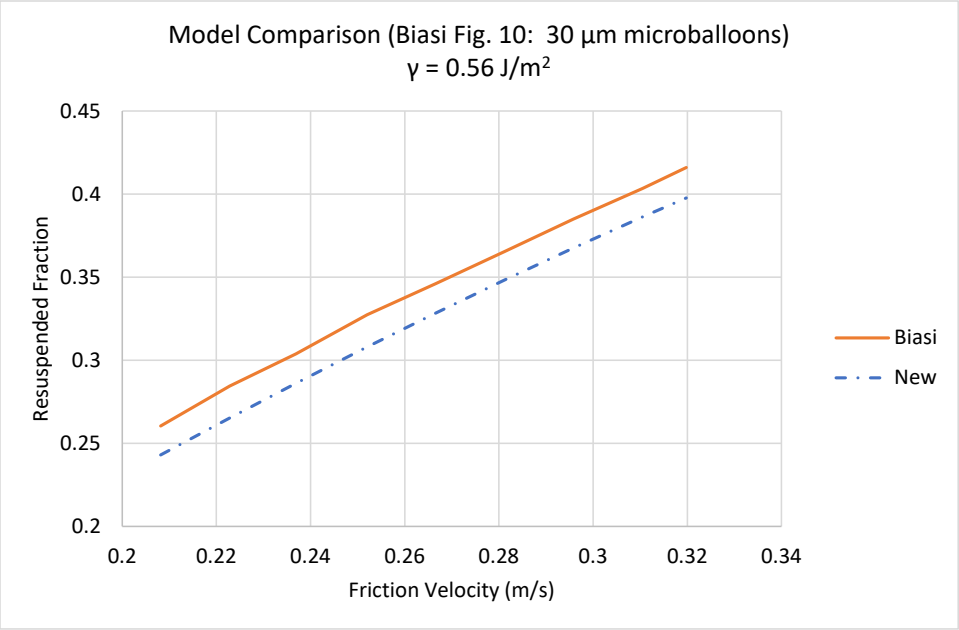


Figure 29. Comparison of Python model output with Biasi, et al. (2001) model results for fraction of 30 µm diameter glass microballoons resuspended from a glass surface by 1 second of exposure to a constant friction velocity flow, assuming a surface adhesion energy of 0.56 J/m².

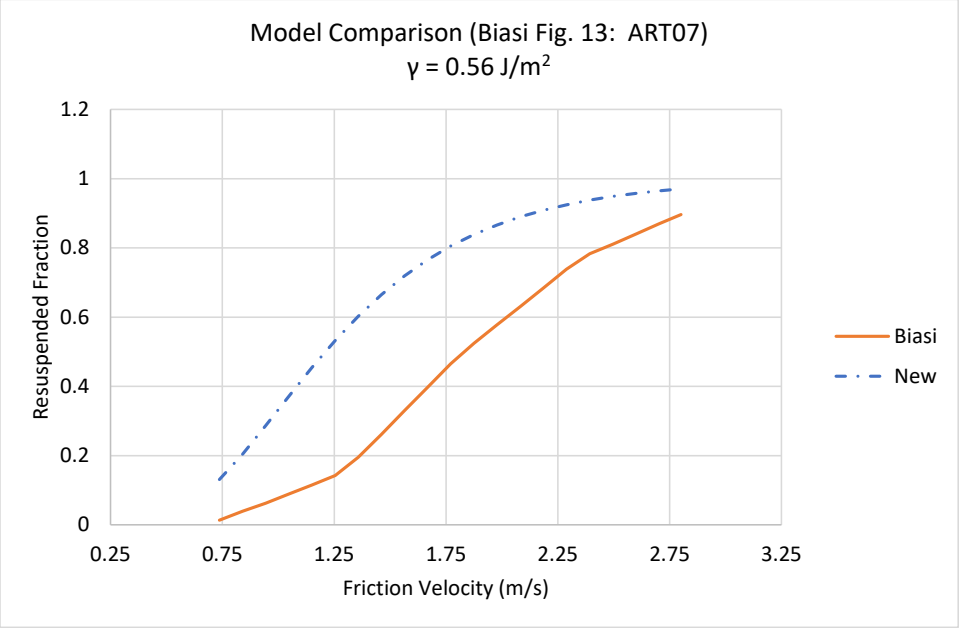


Figure 30. Comparison of Python model output with Biasi, et al. (2001) model results for fraction of 6.37 µm diameter metalic zinc particles resuspended from a flat surface by 1 second of exposure to a constant friction velocity flow, assuming a surface adhesion energy of 0.56 J/m².

Vincent, et al. (2019) documents another implementation of the Reeks and Hall Rock'n'Roll resuspension model. In the Vincent study, the friction velocity is a time-varying quantity that ramps from 0 m/s to approximately 1.3 m/s in 10 seconds and subsequently remains constant.

Vincent, et al. (2019) does not explicitly list all model inputs but does provide particle diameters and citations for references from which they obtained additional parameters, such as surface adhesion energy. Figure 31 shows several bounding results from Vincent, et al. (2019) and overlays new curves generated from the current Python model. The dotted black curve shows the time-varying friction velocity. Vincent perturbed several model inputs to assess the sensitivity of the results, yielding minimum, maximum, and reference (nominal) transient profiles of the fraction of glass particles removed from a doped silicon surface. Experimental measurements were also performed, which are shown in Figure 29 as "Vincent (meas)." Since Vincent did not specify the corresponding surface adhesion energy γ, the Python model was executed using two alternative values: the default 0.56 J/m^2 and 0.067 J/m^2, which was extracted from Farshchi-Tabrizi, et al. (2006), one of several sources cited by Vincent. The various removal fraction transients in Figure 31 exhibit considerable discrepancies. The maximum perturbed model result from Vincent is slower to respond to the friction velocity increase than the experimental data, taking about 5 extra seconds to reach a fraction removed plateau of approximately 0.31. The reference model output from Vincent only reaches a fraction removed plateau of approximately 0.06, whereas the Python model plateaus at 1 when $\gamma = 0.067\ J/m^2$ and 0.75 when $\gamma = 0.56\ J/m^2$. Due to the widespread between the resuspension transients in Figure 31, the new Python implementation of the Reeks and Hall Rock'n'Roll model could not be successfully verified against the data from Vincent. The deviations between the measured, perturbed, and Python-calculated removal fraction curves demonstrate that the results are highly sensitive to the values of the inputs.

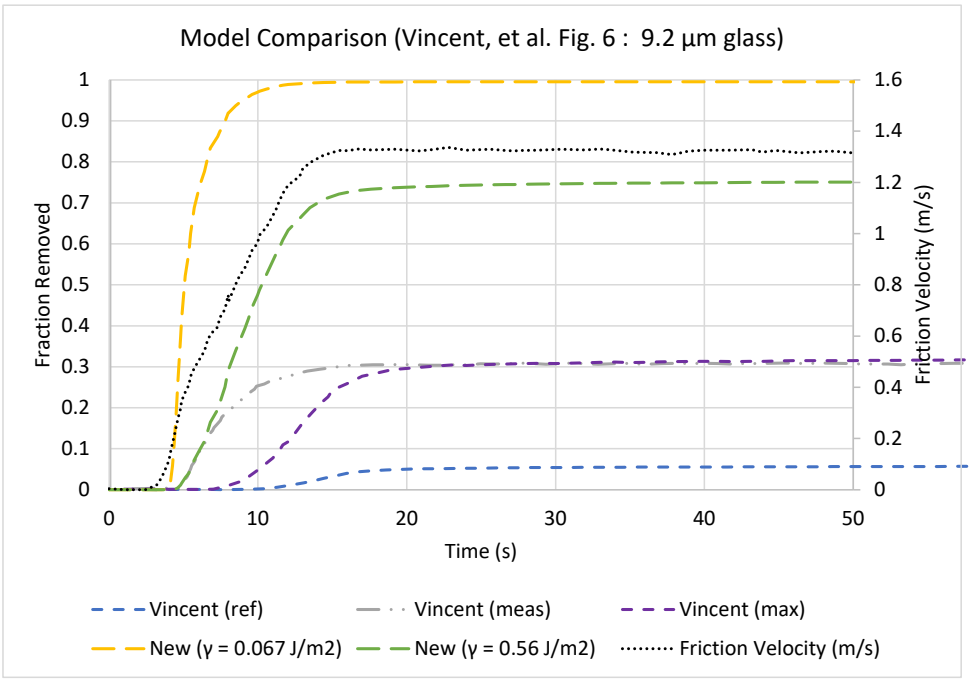


Figure 31. Comparison of Python model output with Vincent, et al. (2019) results for fraction of 9.2 µm diameter glass particles resuspended from a doped silicon surface by exposure to a time-varying friction velocity flow. Since Vincent does not specify input surface adhesion energy, two values are used in the Python model.

6.7 Variation of Pressure on Modeled Particle Resuspension

The effect of pressure on remaining particle fraction N_R is driven by the pressure-dependence of the gas density ρ. The dynamic viscosity μ of an ideal gas has negligible pressure-dependence. Intermediate inputs u_τ, $\langle F' \rangle$, and σ_t are all dependent on density. Using the ideal gas law, changing the gas pressure from P_o to P_1 at constant temperature produces the following changes in density and kinematic viscosity:

$$\frac{\rho_1}{\rho_o} = \frac{P_1}{P_o} \tag{54}$$

$$\frac{\nu_1}{\nu_o} = \frac{P_o}{P_1} \tag{55}$$

Additionally, application of the Blasius correlation [Fox and McDonald, 1985] for turbulent friction factor to the equation suggests the following pressure dependence of friction velocity, under the assumption that freestream velocity is held constant:

$$\frac{u_{\tau 1}}{u_{\tau o}} = \left(\frac{P_o}{P_1}\right)^{0.125} \tag{56}$$

A sample curve showing the effect of gas pressure on a fraction of particles resuspended from a smooth, flat surface after 1 second of exposure to a constant-friction-velocity flow is shown in Figure 32. The input parameters used to generate Figure 32 are presented in Table 3. The freestream velocity of 30.83 m/s was selected to produce a 1.5 m/s friction velocity in a 1.5 inch diameter tube according to equation 53, when using the Blasius correlation [Fox and McDonald] to determine friction factor $\boldsymbol{f}$. This freestream velocity was held constant, regardless of pressure, when generating the curve in Figure 32. In practice, the freestream velocity will likely be affected by changes in pressure unless it is held fixed using a control system. Under these conditions Figure 32 indicates that the fraction of particles removed increases with increasing gas pressure.

Table 3. Inputs for Particle Resuspension Pressure Dependency Analysis

Variable	Value	Units
Mean Particle Diameter	10	µm
Surface Adhesion Energy	0.56	J/m^2
Evaluation Time	1	s
Flow Speed	30.83	m/s
Reference Friction Velocity	1.5	m/s
Reference Pressure	14.7	psia
Flow Diameter	0.0381	m
Dynamic Viscosity	$1.81x10^{-5}$	Pa-s
Ref. Kinematic Viscosity	$1.51\ x10^{-5}$	m^2/s
No. of F'_{asp} Intervals	1000	
No. of F'_{asp} Standard Devs	4	
Pressure:	14.7	psia
Flow Diameter:	1.5	in
Kinematic Viscosity:	$1.51x10^{-5}$	m^2/s
Flow Speed:	30.83	m/s

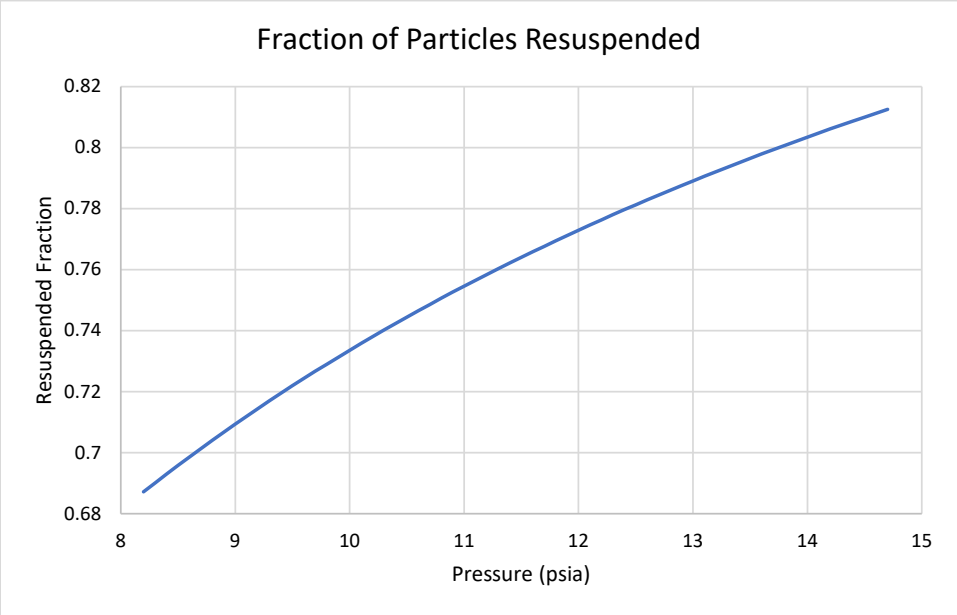


Figure 32. Variation of particle resuspension fraction with gas pressure, subject to the assumed inputs from Table 4.

7 References

1. Biasi, L., de los Reyes, A., Reeks, M. W., and De Santi, G. F., Use of a simple model for the interpretation of experimental data on particle resuspension in turbulent flows. *Aerosol Science*, 32, 1175–1200, 2001.

2. Farshchi-Tabrizi, M., Kappl, M., Cheng, Y., Gutmann, J., and Butt, H-J., On the adhesion between fine particles and nonocontacts: an atomic force microscope study, Langmuir, 22, 2171-2184, 2006.
3. Fox, R. W. and McDonald, A. T., *Introduction to Fluid Mechanics*, 3rd ed., New York: John Wiley & Sons, 1985.
4. Fred A. McAllister, "Apollo Experience Report - Crew Provisions and Equipment Subsystem," NASA, NASA TN D-6737, 1972.
5. Marshal Space Flight Center, "HUMAN LANDING SYSTEM (HLS) PROGRAM SYSTEM REQUIREMENTS DOCUMENT(PSRD)," HLS-RQMT-001, Rev D, Nov 3, 2020.
6. Molly S. Anderson, Michael K. Ewert, and John F. Keener, "Life Support Baseline Values and Assumptions Document," NASA/TP-2015–218570/REV1, January 2018.
7. NASA, "Human Landing System to Orion Interface Requirements Document," HLS-IRD-005, Rev A, January 30, 2020.
8. O. A. Alduchov and R.E. Eskridge, "Improved Magnus form approximation of saturation vapor pressure," *Journal of Applied Meteorology*, vol. 35, no. 4, pp. 601-609, April 1996.
9. O'Neil, M. E., Chemical Engineering Science, 23, 1293-1298, 1968.
10. "Orion Multi Purpose Crew Vehicle (MPCV) Program: Human-Systems Integration Requirements," Requirements Document MPCV 70024 Revision C, July 20, 2016.
11. Reeks, M. W., & Hall, D., Kinetic models for particle resuspension in turbulent flows: Theory and measurement. *Aerosol Science*, 32, 1–31, 2001.
12. Steve A. Lee, "Easy5 Model for HLS-Orion Docked Ops," JETS-JE33-21-TLSS-DOC-0072, 2021.
13. Vincent, J. C., Hill, J., Walker, M. D., Smith, S. A., Smith, S. E., Cant, N. E., Towards a predictive capability for the resuspension of particles through extension and experimental validation of the Biasi implementation of the "Rock'n'Roll" model, Journal of Aerosol Science, 137, 105435, 2019.

8 Recommendation for Future Work

Recommended future work for this test campaign includes:

- Assessment of the debris (lunar dust in this case) discharge rate out of the vacuum cleaner: How much lunar dust is blown back out from the vacuum cleaner after the air/lunar dust flows through any filters, bags, etc.
- Assessment of the vacuum cleaner filter: What happens to the filter as lunar dust particles flow through, does the filter clog at a certain correlatable point, is there damage to the filter that would impair the vacuum or filter from performing its function, etc.
- Assessment of containment method: What is the optimal type of dust collection/containment method, i.e. perform testing of vacuum cleaners that contain dust via a bag, a canister that needs to be dumped, a self-closing method, while performing operations such as moving, lightly shaking, changing dust container, to see what method is best for keeping dust contained when in use, moving, or changing out bags/filters.

9 Acknowledgements

I would like to acknowledge the following people were particularly helpful in the production of this work.

- Vacuum Cleaner Team: Glenn Waguespack, Kristen John
- MEGA Lab: Joanna Clark
- Simulant Development Lab: Sarah Walker, John Gruener
- B31 Microscopy Lab: Lindsay Keller, Kathie Thomas-Keprta

10 Appendix

10.1 Assessment Memo from Building 13 Microscopy Lab

The following is content from the assessment memo received from James Martinez, a lead technologist in the microscopy lab. The text has not been changed, but formatting may have changed slightly to be incorporated in this paper.

2021.08.16

TO: Steve A. Lee, JETS EC111 Thermal Analyst

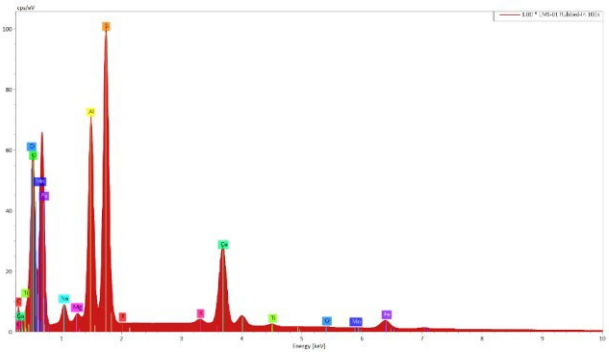
FROM: James E. Martinez, JETS ES181 Engineering Technologist

SUBJECT: Feasibility Study on Particle Analysis of LMS-1 Rubbed-In Ortho Fabric Test Coupon

Purpose:

The purpose of this feasibility study is to compare ES particle analysis capabilities collected with an EDS equipped SEM to a COTS optical microscope particle analyzer fitted with an M-Jet dispersion module.[2] Method:

A 30-minute EDS map is collected at 100x magnification with 921,881 μm^3 area at 20kV accelerating voltage in variable pressure mode (40 Pa) for charge compensation. An element spectrum generated and all peaks are labeled.



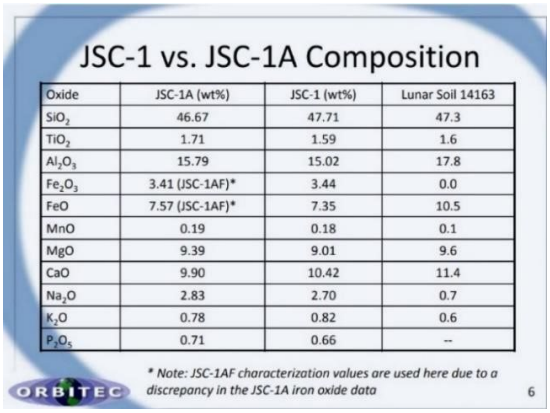
100x EDS Map Overall Spectrum

Per the manufacturer, JSC-1A Lunar Regolith Simulant contains eleven different oxides.[2] It is unknown which simulant was applied to the Ortho fabric test coupons.

---

[2] https://www.microtrac.com/products/particle-size-shape-analysis/static-image-analysis/camsizer-m1/

[3] https://www.nasa.gov/sites/default/files/atoms/files/03_jsc-1a_lunar_regsimulant_update_bgustafson.pdf



JSC-1 vs. JSC-1A Composition

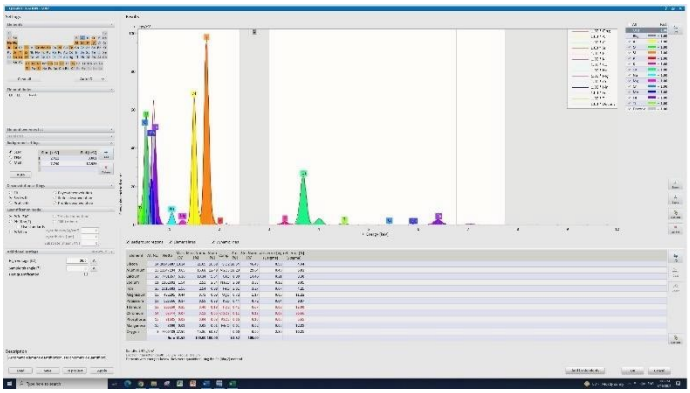
Oxide	JSC-1A (wt%)	JSC-1 (wt%)	Lunar Soil 14163
SiO_2	46.67	47.71	47.3
TiO_2	1.71	1.59	1.6
Al_2O_3	15.79	15.02	17.8
Fe_2O_3	3.41 (JSC-1AF)*	3.44	0.0
FeO	7.57 (JSC-1AF)*	7.35	10.5
MnO	0.19	0.18	0.1
MgO	9.39	9.01	9.6
CaO	9.90	10.42	11.4
Na_2O	2.83	2.70	0.7
K_2O	0.78	0.82	0.6
P_2O_5	0.71	0.66	--

ORBITEC

** Note: JSC-1AF characterization values are used here due to a discrepancy in the JSC-1A iron oxide data*

6

Simulant Composition



Quantification of all oxides except Fe_2O_3

Element	At. No.	Netto	Mass[%]	Mass Norm.[%]	Atom[%]	Comp.	Sto.[%]	Sto. Norm.[%]	abs. error [%](1 sigma)	rel. error [%](1 sigma)
Oxygen	8	7766489	27.90	45.36	60.87		0.00	0.00	2.86	10.25
Silicon	14	20845887	13.34	21.69	16.58	SiO2	28.54	46.40	0.59	4.44
Aluminium	13	13347234	9.65	15.68	12.48	Al2O3	18.23	29.64	0.49	5.03
Calcium	20	7791357	6.36	10.34	5.54	CaO	8.90	14.46	0.21	3.30
Iron	26	1015983	1.56	2.54	0.98	FeO	2.01	3.27	0.07	4.25
Sodium	11	1162992	1.54	2.51	2.34	Na2O	2.08	3.38	0.12	8.05
Magnesium	12	482201	0.44	0.71	0.63	MgO	0.72	1.17	0.05	11.22
Potassium	19	520566	0.37	0.59	0.33	K2O	0.44	0.72	0.04	9.87
Titanium	22	226160	0.25	0.40	0.18	TiO2	0.41	0.67	0.03	13.00
Chromium	24	63544	0.07	0.12	0.05	Cr2O3	0.11	0.18	0.03	36.66
Phosphorus	15	31685	0.03	0.04	0.03	P2O5	0.06	0.10	0.00	5.65
Manganese	25	8000	0.01	0.02	0.01	MnO	0.01	0.02	0.00	12.32
		Sum	61.52	100.00	100.00		61.52	100.00		

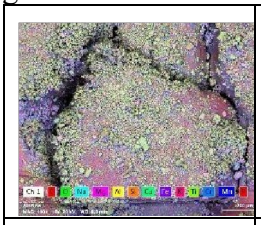
Results:

Quantification results match closely to reported values for some oxides (SiO_2, FeO, Na_2O, K_2O, MnO) but differ significantly for other oxides (Al_2O_3, CaO, MgO, TiO_2). Cr_2O_3 is not reported in Orbitec's analysis but was detected by EDS. EDS is not capable of differentiating between FeO and Fe_2O_3. Only FeO values are reported. Fe_2O_3 is also excluded from Orbitec's quant, so total column does not equal 100%.

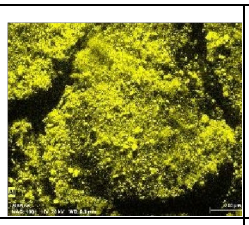
Element	Comp.	Sto. Norm.[%]	Orbitec JSC-1A Wt%
Oxygen		0.00	
Silicon	**SiO2**	46.40	46.67
Aluminium	**Al2O3**	29.64	15.79
Calcium	**CaO**	14.46	9.90
Iron	**FeO**	3.27	3.41
Sodium	**Na2O**	3.38	2.83
Magnesium	**MgO**	1.17	9.39
Potassium	**K2O**	0.72	0.78
Titanium	**TiO2**	0.67	1.71
Chromium	**Cr2O3**	0.18	0.00
Phosphorus	**P2O5**	0.10	0.71
Manganese	**MnO**	0.02	0.19
		100.00	

Quant Results: EDS vs. Orbitec

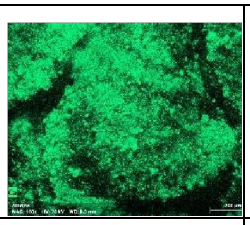
Once all peaks are properly identified and labeled, individual EDS element maps are then generated.



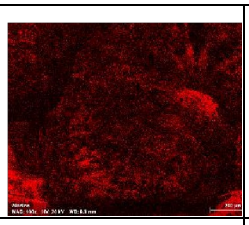
All Elements



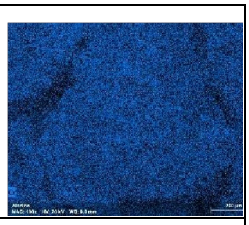
Aluminum



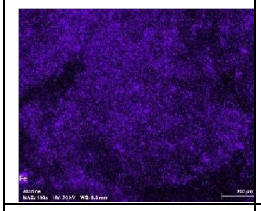
Calcium



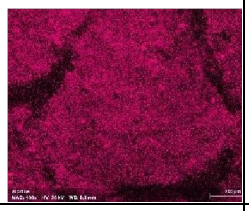
Carbon



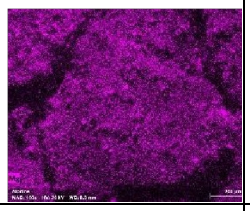
Chromium



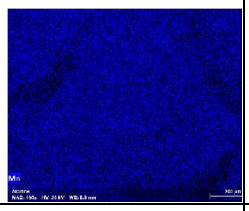
Iron



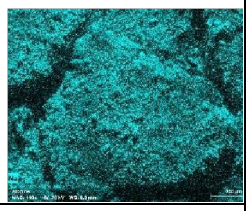
Potassium



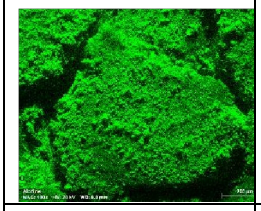
Magnesium



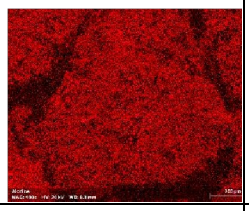
Manganese



Sodium



Oxygen



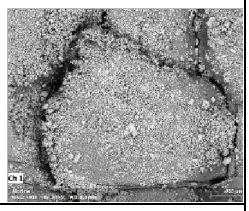
Phosphorus



Silicon



Titanium

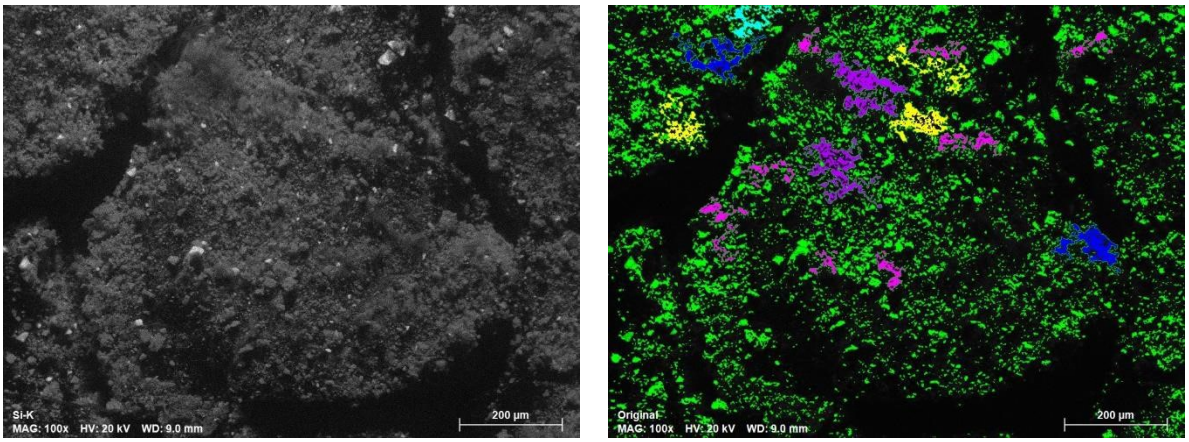


BSE Image

100x EDS Element Map

Each element must selected and analyzed individually for particle counting. For this study, only the SiO_2 EDS map was analyzed and counted. To determine total particle count, all oxides must be analyzed separately and added to produce a total particle count.

A binary image of selected oxide (in this case SiO_2) is imported to "Feature" software.

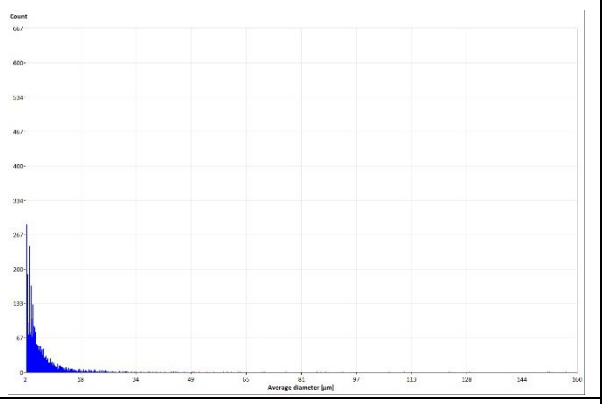


SiO2 Binary Input & Output Images

Particle analysis of SiO_2 reports 4369 particles. There are several large regions in the map data not detectable by EDS due to high topography inherent in a woven fabric structure.

Feature analysis	Field 0	
fields	1	
Image	1024 x 768	pixels
Area	921881	µm²
Particles	4369	
Accepted	4369	

Particle Count Results



Histogram of Particle Ave. Diameter (µm)

Conclusion:

Particle analysis of data collected with an EDS equipped SEM has several advantages over an optical microscope system but significant disadvantages. These pros and cons are summarized in the table below.

Pros of EDS vs. Dedicated Optical Analyzer	**Cons of EDS vs. Dedicated Optical Analyzer**
1. Elemental analysis possible	1. Slow raw data acquisition

2. Electron imaging has higher spatial resolution than optical imaging	2. Particles may move during analysis due to charge build-up
3. EDS can segregate by chemistry	3. Each phase must be analyzed individually
4. Quantification by chemistry possible	5. Particle data from each element must be added to determine total particle count
	6. Ortho fabric susceptible to electron beam damage
	7. Regolith contaminates SEM chamber
	8. No dispersion module is available
	9. Bruker software unable to segregate particles contacting or stacked on top of other particles
	10. High surface topography (woven fabric) results in large regions not detectable by EDS